Mechanism of conductance control and neurosteroid binding in NMDA receptors

https://doi.org/10.1038/s41586-025-09695-4

Received: 19 May 2025

Accepted: 30 September 2025

Hyunook Kang[1], Ruben Steigerwald[1], Elijah Z. Ullman[2], Max Epstein[1], Srinu Paladugu[3], Dennis C. Liotta[3], Stephen F. Traynelis[2,4] & Hiro Furukawa[1]✉

Ion-channel activity reflects a combination of open probability and unitary conductance[1]. Many channels display subconductance states that modulate signalling strength[2,3], yet the structural mechanisms governing conductance levels remain incompletely understood. Here we report that conductance levels are controlled by the bending patterns of pore-forming transmembrane helices in the heterotetrameric neuronal channel GluN1a-2B *N*-methyl-D-aspartate receptor (NMDAR). Our single-particle electron cryomicroscopy (cryo-EM) analyses demonstrate that an endogenous neurosteroid and synthetic positive allosteric modulator (PAM), 24S-hydroxycholesterol (24S-HC), binds to a juxtamembrane pocket in the GluN2B subunit and stabilizes the fully open-gate conformation, where GluN1a M3 and GluN2B M3′ pore-forming helices are bent to dilate the channel pore. By contrast, EU1622-240 binds to the same GluN2B juxtamembrane pocket and a distinct juxtamembrane pocket in GluN1a to stabilize a sub-open state whereby only the GluN2B M3′ helix is bent. Consistent with the varying extents of gate opening, the single-channel recordings predominantly show full-conductance and subconductance states in the presence of 24S-HC and EU1622-240, respectively. Another class of neurosteroid, pregnenolone sulfate, engages a similar GluN2B pocket, but two molecules bind simultaneously, revealing a diverse neurosteroid recognition pattern. Our study identifies that the juxtamembrane pockets are critical structural hubs for modulating conductance levels in NMDAR.

Many ion channels exhibit subconductance states that fine-tune ion flows and subsequent downstream cellular signalling. NMDARs are also known to display multiple conductance states[2,3], suggesting the presence of multiple open conformations with distinct permeabilities that contribute to neuronal activity regulation[4–6]. However, the mechanism of the conductance control is not well understood. NMDARs are ligand-gated ion channels that have a pivotal role in neurotransmission and plasticity, essential for learning and memory[7,8]. They are heterotetrameric receptors composed of two glycine-binding GluN1 subunits and two glutamate-binding GluN2 subunits (GluN2A–D)[9–11]. The opening of the NMDAR channel requires concurrent binding of glycine to the GluN1 ligand-binding domain (LBD) and glutamate to the GluN2 LBD during neurotransmission, and the postsynaptic membrane must be depolarized to relieve the Mg^{2+} block within the transmembrane domain (TMD)[12–15]. Once the central pore formed by the GluN1a M3 and GluN2B M3′ helices opens, the NMDAR channel conducts Na^+ and Ca^{2+} influx and K^+ efflux, with Ca^{2+} entry having a key role in initiating downstream neuroplastic signalling[16].

Over the past three decades, numerous modulators of NMDARs have been identified, including neurosteroids that are naturally present in the brain[17,18]. These endogenous compounds regulate neuronal activity, and deficiencies in their levels have been linked to various neurological and psychiatric disorders, such as anxiety, depression, epilepsy and neurodegenerative diseases[17]. Neurosteroids exert many of their effects by modulating ligand-gated ion channels, including GABAA receptors and NMDARs, thereby influencing synaptic transmission, neuronal excitability and plasticity[19]. Two classes of neurosteroids—pregnenolone sulfate (PS), a sulfated steroid, and 24S-hydroxycholesterol (24S-HC), a hydroxylated cholesterol derivative predominantly present in the brain—have been shown to enhance NMDAR activity[20]. Hydrophobic compounds similar in size to neurosteroids are a class of synthetic modulators known as EU1622 that potentiate NMDAR channel activity by increasing the open probability (P_o) while stabilizing a subconductance state[21–23]. However, the modulator binding sites and the mechanistic understanding of potentiation remain unclear. Here we show that the neurosteroids PS and 24S-HC bind distinctively to the juxtamembrane pockets in the GluN2B subunit, where two PS molecules bind per subunit and one 24S-HC molecule binds per subunit, overlapping with one of the two PS-binding sites. 24S-HC stabilizes the fully open state, in which pore-forming GluN1a M3 and GluN2B M3′ helices bend and widen the channel gate. EU1622-240 has two binding sites, one similar to 24S-HC and the other located in a juxtamembrane pocket in GluN1a that prevents GluN1a M3 from bending. The single-channel recordings on 24S-HC and EU1622-240 indicate the full conductance

---

[1]W.M. Keck Structural Biology Laboratory, Cold Spring Harbor Laboratory, Cold Spring Harbor, NY, USA. [2]Department of Pharmacology and Chemical Biology, Emory University School of Medicine, Atlanta, GA, USA. [3]Department of Chemistry, Emory University, Atlanta, GA, USA. [4]Neurodegenerative Disease Center, Emory University School of Medicine, Atlanta, GA, USA. ✉e-mail: furukawa@cshl.edu

and subconductance levels, indicating that the two structural patterns of channel opening regulate the conductance states.

Channel regulation by neurosteroids

The natural neurosteroids 24S-HC and PS have hydrophobic cholesterol backbones, similar in size to the synthetic compound EU1622-240 (Fig. 1a). All three compounds allosterically potentiate the channel activity, therefore serving as PAMs[22–26]. At the single-channel level, both 24S-HC and PS enhance the activity of GluN1a-2B NMDAR by increasing the channel P_o (Fig. 1b and Supplementary Table 1). With 0.5 mM $CaCl_2$ and 150 mM NaCl in the external solution, the channel predominantly exhibits a full conductance state (around 65 pS chord conductance/90%) with an occasional subconductance level (about 54 pS/10%) (Fig. 1b). While numbers of conductance levels have been reported depending on the extracellular calcium concentrations, the observation of the two conductance levels at 0.5 mM $CaCl_2$ are consistent with the previous reports[21,27–30]. Addition of 24S-HC or PS does not detectably alter the conductance level, indicating that the neurosteroid binding induces intrinsic channel opening with a higher P_o. By contrast, EU1622-240 upregulates channel activity by increasing the P_o (Fig. 1b), but it stabilizes subconductance states (40 pS/75% and 56 pS/25%), indicating that it may not fully induce the channel opening. These observations led to a hypothesis that binding sites for these compounds may have a role in regulating conductance levels.

PS and 24S-HC bind distinctly at the TMD

We attempted to identify binding sites for PS and 24S-HC by obtaining cryo-EM structures of GluN1a-2B NMDAR in a complex with agonists and either PS or 24S-HC (Fig. 2a,b). To capture binding patterns of these neurosteroids (Extended Data Figs. 1 and 2 and Supplementary Table 2), we implemented 3D classification followed by local refinement of the TMD region. Both PS and 24S-HC bind to the juxtamembrane pockets, surrounded by GluN1a M3, and GluN2B Pre-M1′, M1′, M2′ and M4′ helices (Fig. 2a,b (right)). The PS-bound structure revealed that the two binding pockets, site-1 and site-2, are occupied by two PS molecules in distinct binding modes, resulting in a total of four PS-binding sites in the GluN1a-2B heterotetramer (Fig. 2a). The sterol-ketone backbones of the two PS molecules are within 4 Å of one another and surrounded by GluN2B (Leu551, Trp559, Trp610, Trp614, Tyr823 and Met824) and GluN1a (Val635, Gly638 and Ile642) to form hydrophobic interactions (Fig. 2a (right)). The sulfate groups point out towards the extracellular space, of which the one in site-2 interacts with GluN2B Tyr823 (Fig. 2a). The site-2 PS is placed roughly orthogonal to the membrane plane, whereas the site-1 PS is tilted relative to site-2 PS by around 30° (Fig. 2a).

In contrast to PS, one 24S-HC binds to site-1 but not to site-2, resulting in a total of two 24S-HC-binding sites per GluN1a-2B NMDAR tetramer. Parts of site-1 and site-2 are occupied by phospholipid acyl chains, which also interact with 24S-HC (Fig. 2b). 24S-HC directly interacts closely with similar hydrophobic residues to PS but more extensively with the ones from GluN2B M1′ and M2′ (Fig. 2b). A notable feature of the 24S-HC binding is the hydrogen bond between the 24S hydroxyl group of 24S-HC and the main chain carbonyl of GluN2B Phe563 in the TMD, which affects the local architecture of the GluN2B M1′ helix. The lipid acyl chains in site-1 and site-2 are surrounded by GluN1a Val635, Gly638 and Ile642, and GluN2B Trp610, Phe614 and Met824 (Fig. 2b).

To validate the PS- and 24S-HC-binding sites observed in the cryo-EM structures, we tested the site-directed mutants for their potentiating effects of PS and 24S-HC using two-electrode voltage-clamp (TEVC) electrophysiology (Fig. 2c,d). Mutations of the directly interacting residues affected the extent of potentiation by PS ($I(\mathrm{PS})/I_0$) compared with the wild-type (WT) receptor. GluN1a(Val635Ala) showed increased potentiation, while all the other mutants displayed decreased potentiation (Fig. 2c). For 24S-HC, the pre-M1′ mutant, GluN2B(Leu551Ser), showed a significant increase in potentiation ($I(\mathrm{24S\text{-}HC})/I_0$) while the M2′ mutant, GluN2B(Trp610Ala), displayed a decreased level of potentiation compared to the WT receptor (Fig. 2d). The single point mutations of residues on GluN1a M3, GluN2B M1′ and GluN2B(Ile606Ala) on GluN2B M2′ did not alter the potentiation effects significantly. GluN2B(Phe614Ala) and GluN2B(Met824Ala), which are in direct contact with the phospholipid acyl chains but not 24S-HC, showed decreases in the potentiating effects, indicating that bindings of the lipid and 24S-HC may be cooperative (Fig. 2d). Overall, the site-directed mutagenesis results are consistent with the structural observations that show distinct binding modes between PS and 24S-HC.

We further validated the distinct binding patterns between PS and 24S-HC by testing the additive effects of 24S-HC at various PS concentrations (0–50 μM). While there were minor changes in the 24S-HC half-maximum effective concentration (EC_{50}) values, the extent of potentiation increased with higher PS concentration, possibly indicating synergistic effects (Extended Data Fig. 3a,b).

24S-HC stabilizes the open gate

The 24S-HC-bound GluN1a-2B NMDAR structures are captured with closed and open gates at the extracellular entrance, with cryo-EM density for 24S-HC resolved in both states (Extended Data Fig. 2b,c). Importantly, the channel gate of the 24S-HC-bound GluN1a-2B NMDAR is wider than that captured in the presence of EU1622-240 (refs. 22,31) (Fig. 3a). This broader opening stems from the bending of both GluN1a M3 and GluN2B M3′ helices in the 24S-HC-bound structure, in contrast to the EU1622-240-bound structure, in which only the GluN2B M3′ helices are bent (Fig. 3a (bottom, arrows)). The GluN2B LBD–M3′ linker tension, which is crucial for ligand gating of NMDAR, is similar between the 24S-HC-bound and EU1622-240-bound structures, and substantially lower in the closed state, as measured by the distances between GluN2B Gln662 (Fig. 3a (top); 49.3 Å, 64.1 Å and 63.6 Å for the closed, 24S-HC-bound fully open and EU1622-240-bound sub-open states, respectively). On the basis of the single-channel recordings, in which 24S-HC retains the full conductance while EU1622-240 stabilizes the subconductance state (Fig. 1b), we propose that the 24S-HC-bound structure represents the fully open gate, whereas the EU1622-240-bound structure may represent the sub-open gate (Fig. 3).

In the closed state, the entrance of the channel gate (VIVI-gate) is locked by a cluster of hydrophobic residues—GluN1a Val656 and Leu657 and GluN2B Ile655 (Fig. 3a (left, spheres)). The hydrophobic interactions are disrupted by the GluN2B LBD-M3′ loop tension caused by glutamate binding to the GluN2B LBD[22,31–33], which facilitates bending of the GluN2B M3′ helices (Fig. 3a (bottom middle, arrows)). In this channel-opening step, the GluN2B pre-M1′ and the connecting loops move to accommodate the bent GluN2B M3′ helices (Fig. 3b (left, dotted arrows 1–2)). The 24S-HC (Fig. 3b (middle, asterisk)) interacts with the GluN2B pre-M1′ region to favour this process (Extended Data Fig. 4a). The GluN2B M3′ bending is accompanied by movement of the GluN1a LBD-M4 loop and pre-M1, as represented by the substantial positional change of GluN1a Leu551 (Fig. 3b (left, dotted arrows 3–4; and right, dotted arrow). These concerted rearrangements create the space to accommodate the bent GluN1a M3 (Fig. 3b). In this fully open conformation, the hydrophobic residues at the VIVI gate (GluN1a Val656 and Leu657, and GluN2B Ile655) interact with new sets of residues, GluN1a Ala806/Leu808 (pre-M4) and GluN2B Val545/Leu813 (pre-M1′/pre-M4′) (Fig. 3a,b (spheres, light pink and light cyan)). The primary determinant of ligand gating in ionotropic glutamate receptors (iGluRs) is the increased tension in the GluN2B LBD-M3′ loop, evidenced by the greater distance between the two GluN2B Gln662 residues in the open state compared with in the closed state (Fig. 3a and Extended Data Fig. 4b). By contrast, the positions of the corresponding GluN1a LBD-M3 loop residue GluN1a Ile664 remain mostly unchanged, indicating minimal alteration in the loop tension in GluN1a (Extended Data Fig. 4b).

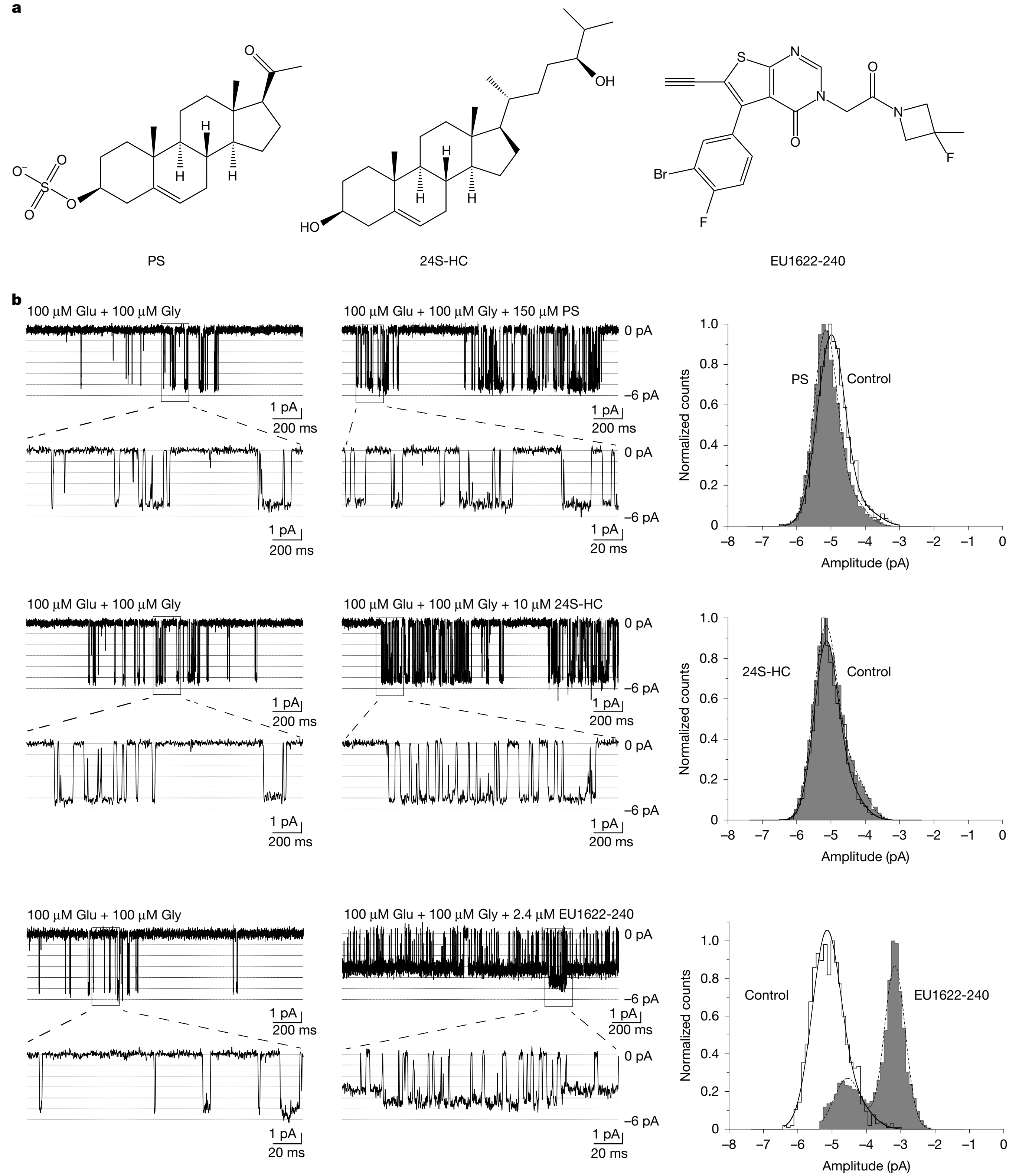

Fig. 1 | Neurosteroids and EU1622-240 upregulate GluN1a-2B NMDAR activity. **a**, The chemical structures of PS, 24S-HC and EU1622-240. Note that EU1622-240 has a similar size and hydrophobicity to PS and 24S-HC. **b**, Representative single-channel unitary currents of GluN1-2B NMDAR in the absence or presence of PS, 24S-HC or EU1622-240 at −80 mV holding potential in the outside-out configuration. Here, current responses were filtered at 1 kHz (−3 dB) using a Gaussian filter. The regions indicated by the box and the dashed lines show currents on an expanded time base. Representative amplitude histograms of the unitary current amplitudes are shown for the patches. The unitary current amplitudes for the representative control recordings at −80 mV for PS, 24S-HC and EU1622-240 were as follows: PS control: −5.0 pA, 93%; −3.9 pA, 7%; 24S-HC control: −5.2 pA, 89%; −4.3 pA, 11%; and EU1622-240 control: −5.2 pA, 91%; −4.2 pA, 9%. The unitary current amplitudes for PS, 24S-HC and EU1622-240 representative recordings at −80 mV were as follows: PS: −5.2 pA, 90%; −4.3 pA, 10%; 24S-HC: −5.1 pA, 83%; −4.4 pA, 17%; and EU1622-240: −4.6 pA, 29%; −3.2 pA, 71%. The control histogram is shown in white, and PS, 24S-HC and EU1622-240 histograms are shown in grey. The amplitude histograms were fitted by two Gaussian functions (smooth lines and dashed lines) and the result of the fit is summarized in Supplementary Table 1.

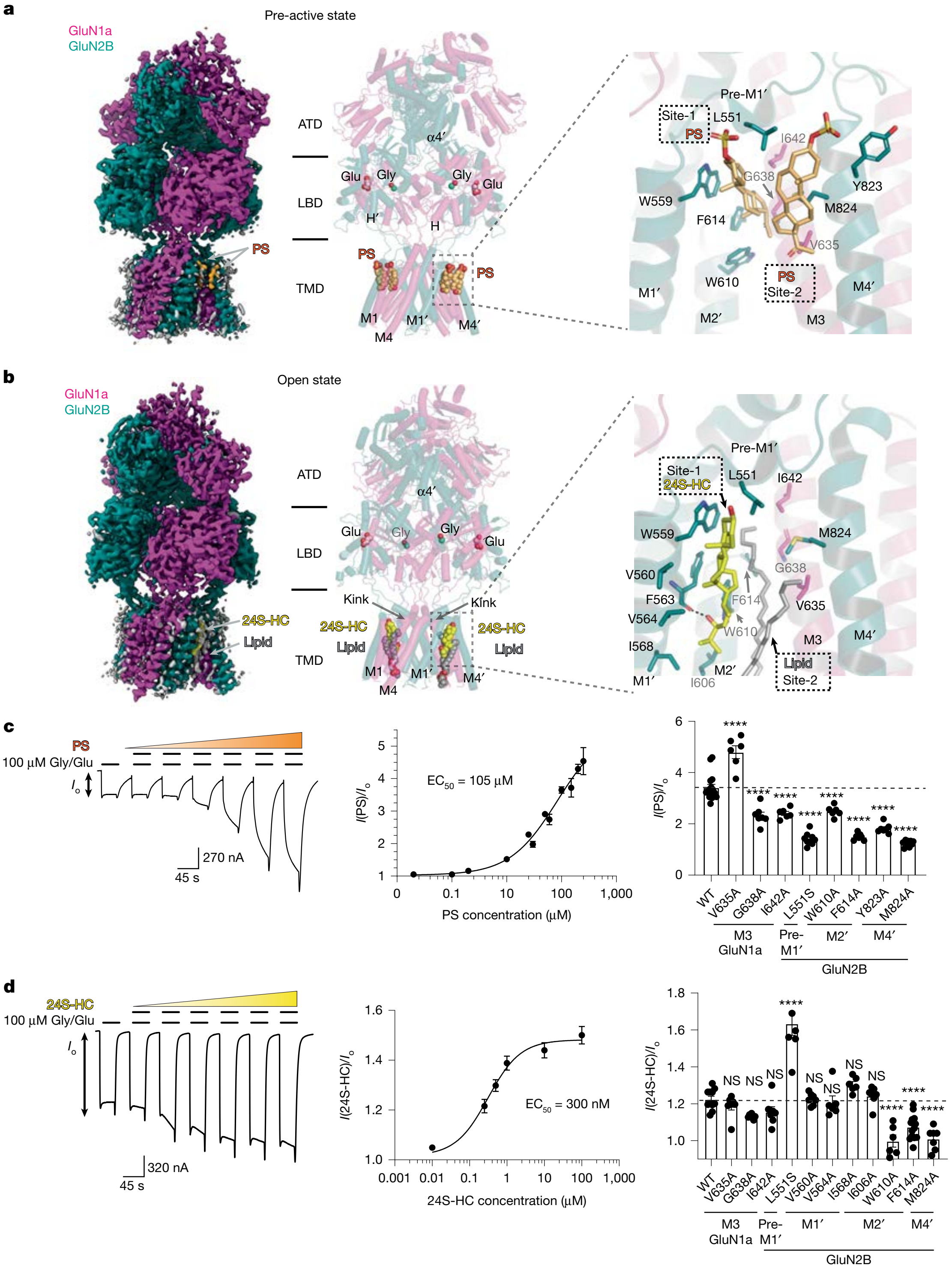

Fig. 2 | Structures of GluN1a-2B NMDARs in a complex with PS and 24S-HC. **a**, Cryo-EM density and structural models of the PS-bound GluN1a-2B NMDAR. Bound Gly, Glu and PS are shown as spheres; PS is coloured in light orange (left). Right, the magnified view shows the PS-binding site at the GluN2B juxtamembrane pocket, showing two PS molecules, site-1 and site-2, and interacting residues. ATD, amino-terminal domain. **b**, Cryo-EM density and structural models as in **a**, but for the 24S-HC-bound GluN1a-2B NMDAR. 24S-HC and the associated lipid are shown as yellow and grey spheres, respectively (left). Right, magnified view of the binding site, showing 24S-HC at site-1 and the lipid in the portion of the site-2 pocket. **c**,**d**, Structure-based site-directed mutagenesis at the PS- and 24S-HC-binding sites. Representative concentration response curves and plots of PS (**c**) and 24S-HC (**d**) obtained by TEVC recordings from independent oocytes. *n* = 12 (PS) and *n* = 14 (24S-HC). The 95% confidence interval (CI) for PS was 56.4–824.0 μM; and for 24S-HC, 166–468 nM. The Hill slope for PS was 0.9; and for 24S-HC, 0.87. Potentiation was calculated as the fold increase in current (I(PS) or I(24S-HC)) relative to the Gly/Glu current (I_o). The mutational effects were measured using 150 μM PS or 10 μM 24S-HC. The mutated regions are indicated along the *x* axis. Data are mean ± s.e.m. from independent oocytes. PS: *n* = 16 (WT), *n* = 6 (GluN1: V635A, I642A), *n* = 7 (GluN1: G638A), *n* = 6 (GluN2B: W610A), *n* = 7 (GluN2B: F614A, Y823A), *n* = 9 (GluN2B: L551S, M824A); 24S-HC: *n* = 11 (WT), *n* = 7 (GluN1: V635A, G638A, I642A), *n* = 6 (GluN2B: V564A, I568A, W610A), *n* = 7 (GluN2B: L551S, V560A, I606A, M824A), *n* = 14 (GluN2B: F614A). Statistical significance was assessed using one-way analysis of variance (ANOVA) followed by Dunnett's test (two-sided) comparing each group with the WT. *P* values were adjusted for multiple comparisons with family-wise $\alpha = 0.05$. ****$P < 0.0001$; NS, not significant.

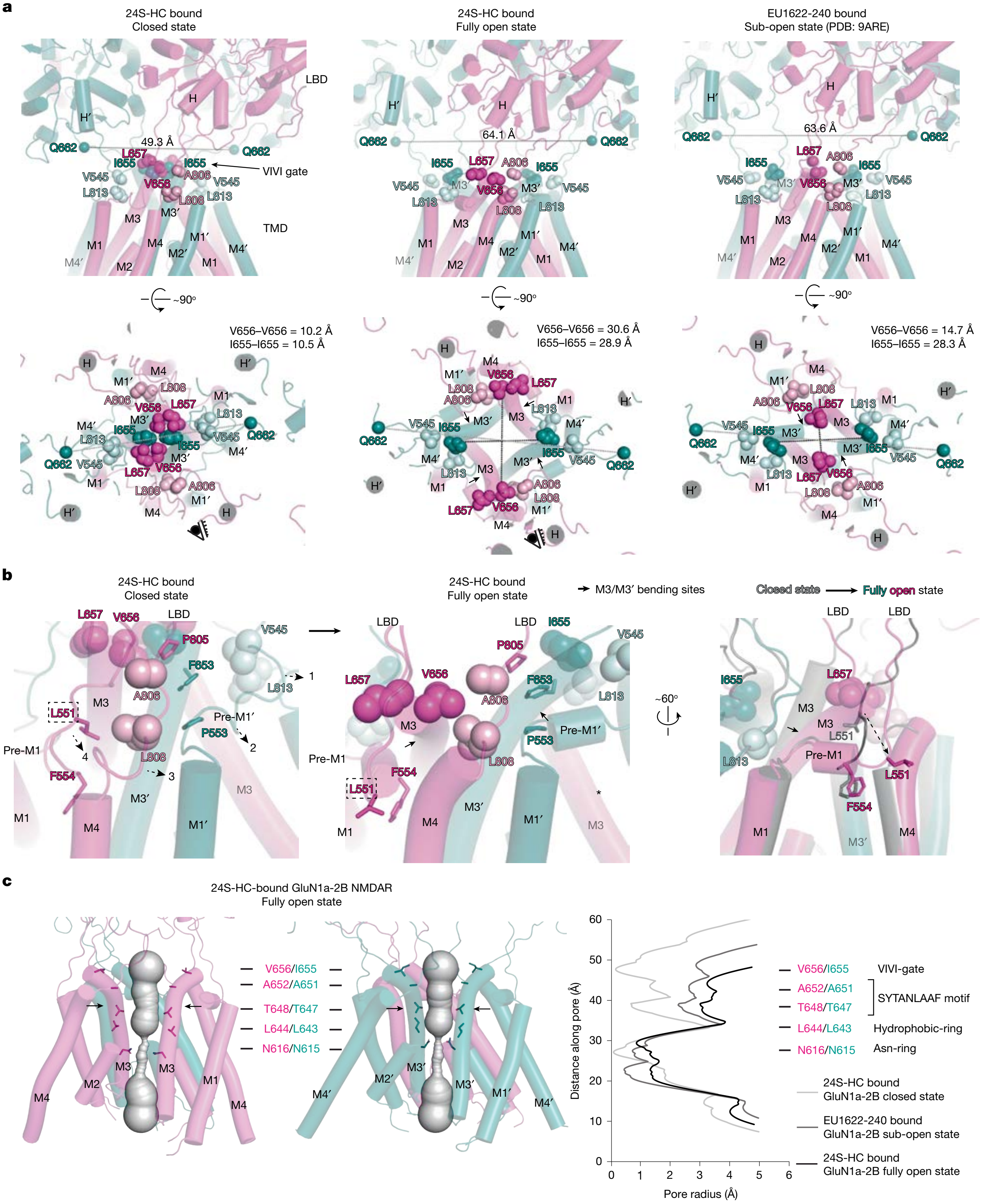

Fig. 3 | 24S-HC stabilizes the fully open gate. a, Comparison between the 24S-HC-bound structures in the closed and open gate and the EU1622-240-bound structure (PDB: 9ARE) viewed from the side (top) and top (bottom) of the TMDs, showing different extents of the gate opening. GluN2B LBD-M3′ loop tension was quantified as the distance between the α carbons of GluN2B Gln662 (spheres). The hydrophobic gate residues are shown as magenta and deep teal spheres, and the interacting residues in the open state are coloured light pink (GluN1a) and light cyan (GluN2B). **b**, The structural hub for channel gating, showing the sequential movement crucial for full channel opening (dotted arrow 1–4; left). The GluN2B pre-M1′ loop, GluN1a M4 and GluN1a pre-M1 move to accommodate the bending of GluN1a M3 and GluN2B M3′ (short arrows; middle and right). The superposition of fully open (magenta and deep teal) and closed (grey) structures demonstrates a pronounced GluN1a pre-M1 movement represented by the GluN1a Leu551 positions (dotted arrow; right). **c**, HOLE analysis of the 24S-HC bound GluN1a-2B NMDAR in the fully open state. A wider dilation of pore radius is observed around the VIVI-gate compared with the closed state and sub-open state (EU1622-240-bound). The arrows on the models represent the kinked region of the GluN1a M3 and GluN2B M3′ helices.

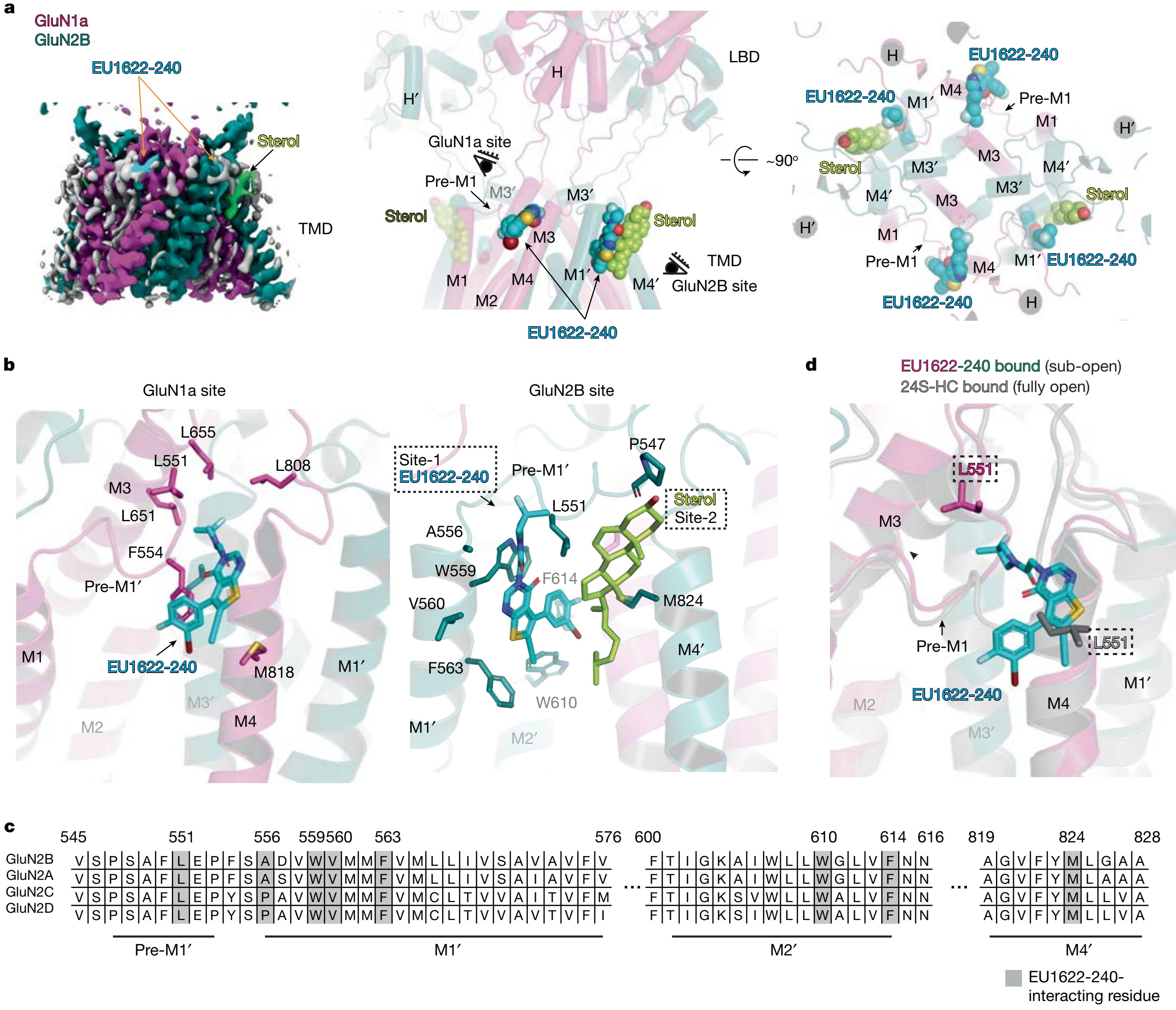

545 551 556 559 560 563 576 … 600 610 614 616 … 819 824 828

GluN2B V S P S A F L E P F S A D V W V M M F V M L L I V S A V A V F V … F T I G K A I W L L W G L V F N N … A G V F Y M L G A A
GluN2A V S P S A F L E P F S A S V W V M M F V M L L I V S A I A V F V … F T I G K A I W L L W G L V F N N … A G V F Y M L A A A
GluN2C V S P S A F L E P Y S P A V W V M M F V M C L T V V A I T V F M … F T I G K S V W L L W A L V F N N … A G V F Y M L L V A
GluN2D V S P S A F L E P Y S P A V W V M M F V M C L T V V A V T V F I … F T I G K S I W L L W A L V F N N … A G V F Y M L L V A

Fig. 4 | Sub-open structures are stabilized by binding of EU1622-240 at two locations. a, Cryo-EM density of the TMD region of the EU1622-240-bound GluN1a-2B NMDAR. There are two binding sites of EU1622-240 (cyan density of spheres), one in GluN1a and the other GluN2B, totalling four molecules per tetramer. The GluN2B site also contains sterol (lime green density and spheres), which is arbitrarily modelled as cholesterol in this figure. **b**, Magnified views of the EU1622-240-binding sites in GluN1a and GluN2B, showing different binding modes. In GluN2B, EU1622-240 occupies the site equivalent to site-1 in the PS- and 24S-HC-binding sites, whereas sterol occupies site-2. **c**, Sequence alignment of GluN2 subunits at the EU1622-240-binding region. Residues interacting with EU1622-240 are highlighted in grey. Most interacting residues are conserved across subunits, except for Ala556, which is replaced by Pro in GluN2C and GluN2D. **d**, Superposition of sub-open (EU1622-240-bound, magenta and deep teal) and fully open (24S-HC-bound, grey) structures, illustrating the positional overlap of GluN1a Leu551 in pre-M1 and EU1622-240. This demonstrates that EU1622-240 prevents rearrangement of GluN1a pre-M1 necessary for the GluN1a M3 bending.

The GluN2B M3′ bending pattern is highly similar between the EU1622-240-bound[22] and the 24S-HC-bound structures (Fig. 3a (middle and right)). However, the movement in GluN1a LBD-M4 loop and pre-M1 was not observed; the reason for this is explained by the EU1622-240-bound GluN1a-2B NMDAR with improved resolution in the next section (Fig. 4).

The channel pore analysis performed using HOLE[34] revealed a more pronounced opening of the VIVI-gate and SYTANLAAF motif in the 24S-HC-bound form than in the EU1622-240-bound structure and the closed state (Fig. 3c and Extended Data Fig. 5a,b). This pore expansion accommodates an increased number of water molecules that are networked (Extended Data Fig. 6). In the 24S-HC-bound open structure, the M3/M3′ helices are kinked at GluN1a Thr648 and GluN2B Thr647 (Thr-ring), disrupting the α-helical structure and exposing the backbone. This enables the backbone carbonyl group to interact with surrounding waters, forming a water network near the SYTANLAAF motif (Extended Data Fig. 6a). The EU1622-240-bound structure has fewer waters compared with the 24S-HC, consistent with the intermediate pore dimension (Extended Data Fig. 6a). Potential of mean force (PMF) calculations also suggest that the wider opening of the SYTANLAAF motif in the 24S-HC-bound open structure makes Na^+ interaction less favourable (around 1.7 kcal mol^{-1}) compared with the EU1622-240-bound structure (around −2 kcal mol^{-1}) at the equivalent position (Extended Data Fig. 5c (around 15 Å reaction coordinate) and Supplementary Fig. 1). The modest PMF values around the SYTANLAAF motif in the 24S-HC-bound open structure imply a reduced permeation barrier at this gate, consistent with a higher conductance level. While the upper gate, composed of the VIVI-gate and SYTANLAAF motif, is substantially wider in the 24S-HC-bound structure, the narrowest constriction in the permeation pathway around the Asn-ring is similar to the EU1622-240-bound sub-open structure (Fig. 3c and Extended Data Fig. 5a,b). This region has recently been shown to serve as the second gate[35], and may therefore undergo greater dilation than observed in our current structures.

Finally, while the 24S-HC-bound structure was stabilized in a mixture of the open and closed states, the PS-bound structure was confined to the closed state, predominantly adopting the non-active and pre-active conformations[32,33] (Extended Data Fig. 7). In the non-active conformation, the GluN1a-2B LBD dimers are rotated downwards towards the membrane, relieving tension in the GluN2B LBD-M3′ loop, crucial for ligand-gating (Extended Data Fig. 7 (left)). By contrast, in the pre-active conformation, the GluN1a-2B LBD dimers rotate upward relative to the non-active form, increasing tension in the GluN2B LBD-M3′ loop, although not to a degree that is sufficient to trigger gate opening (Extended Data Fig. 7 (left)). 24S-HC and PS bind to a similar juxtamembrane pocket in GluN2B and potentiate the channel function; however, our structures do not explain why the channel conformations are different. The potency of 24S-HC is substantially higher than PS; 24S-HC may therefore have stabilized the open gate more effectively under the cryo-EM condition.

EU1622-240 stabilizes a sub-open state

The EU1622-240-bound structure adopts a sub-open conformation in which the GluN2B M3′ helices are bent, but the GluN1a M3 helices are not[22] (Fig. 3a). This aligns with the unique ability of EU1622-240 to stabilize the subconductance state; however, the underlying mechanism has remained unclear because the precise binding site could not be resolved in the previous study, owing to limited resolution at putative binding region[22]. Here, our improved protocol for effectively binding EU1622-240 to the NMDAR protein sample (Methods), combined with a single-particle analysis workflow that locally refines and 3D classifies the TMD region (Extended Data Fig. 8 and Supplementary Table 2), enabled unambiguous identification of the EU1622-240-binding sites within the juxtamembrane pockets (Fig. 4a).

Our analysis revealed that EU1622-240 binds to both GluN2B and GluN1a at the distinct juxtamembrane pockets, yielding four binding sites per tetramer (Fig. 4a). The EU1622-240-binding site in GluN2B is equivalent to site-1, where the neurosteroids PS and 24S-HC bind (Figs. 2a,b and 4b (right)). Site-2 in this pocket is consistently filled by a sterol-like molecule, probably carried over from the expression host cells (Fig. 4a). In the 24S-HC-bound structure, a phospholipid occupies part of site-2 (Fig. 2b), suggesting that the lipid type at site-2 may influence the binding preferences of 24S-HC and EU1622-240. The GluN1a pocket is formed by residues from GluN1a pre-M1, M3 and M4 (Fig. 4b (left)). In both cases, hydrophobic interactions are the major driver for the binding; however, the interaction modes in the GluN1a and GluN2B binding sites are distinct from each other. The interacting residues are conserved among GluN2(A–D) subunits, except at the 556 position (Fig. 4c), indicating that EU1622-240 may be able to bind to all NMDAR subtypes containing GluN2 subunits. Closely related compounds, EU1622-1 and EU1622-14, have been shown to display PAM enhancement of the maximal current response of GluN2B, GluN2C and GluN2D-containing NMDAR, but have minimal if any effect on the maximal response amplitude of GluN2A-containing NMDARs[21].

Importantly, the EU1622-240 binding to the GluN1a site prevents GluN1a M3 helices from bending, leaving the channel in the sub-open state in which only the GluN2B M3′ helices are bent (Fig. 4a). Consistent with the partial opening, EU1622-240 reduces Ca^{2+} permeability relative to monovalent ions (Extended Data Fig. 9 and Supplementary Table 3), suggesting that the unbent GluN1a M3 hinders Ca^{2+} permeation. Specifically, this binding pocket in the 24S-HC-bound fully open state is occupied by the GluN1a pre-M1 residues, such as GluN1a Leu551 (Fig. 4d), a necessary arrangement to allow GluN1a M3 helices to bend as mentioned above (Fig. 3b). Instead, in the EU1622-240-bound structure, EU1622-240 interacts with GluN1a Leu551 to place the pre-M1 towards the GluN1a M3 helices to prevent its bending. The mechanism of channel potentiation by EU1622-240 resembles that of 24S-HC in GluN2B, which places the GluN2B pre-M1′ in a position to allow bending of the GluN2B M3′ helices for the channel gate opening[22] (Fig. 3b and Extended Data Fig. 4a).

Discussion

Here we elucidate the molecular mechanism of WT NMDAR conductance regulation by revealing distinct channel conformations associated with full and subconductance states. These discrete conformations were resolved through the binding of an endogenous neurosteroid, 24S-HC, and a synthetic PAM, EU1622-240, to previously uncharacterized juxtamembrane pockets, stabilizing the fully open and sub-open states. Given that single-channel recordings indicate that 24S-HC and EU1622-240 promote full and subconductance levels, respectively, it is reasonable to associate these conformations with full and subconductance states (Fig. 5a). Our findings further suggest that these binding pockets could be strategically targeted to modulate NMDAR activity for therapeutic intervention.

The fully open NMDAR structure revealed pronounced bending of the pore-forming GluN1a M3 and GluN2B M3′ helices. By contrast, the sub-open state stabilized by EU1622-240 exhibited bending only in the GluN2B M3′ helices. Our single-particle cryo-EM analysis identified two EU1622-240-binding sites: one at the neurosteroid-binding site in GluN2B and the other at a GluN1a site that effectively prevents GluN1a M3 helices from bending. Thus, EU1622-240 uniquely stabilizes the subconductance state at the GluN1a site while enhancing the P_o at the GluN2B site, resulting in net potentiation. This dual binding mode suggests that the secondary GluN1a site could be selectively targeted to attenuate NMDAR activity. EU1622-240 mediates two subconductance states: a predominant state at 40 pS and a minor state at 56 pS (Fig. 1b). Our single-particle analysis captured only one sub-open conformation in the presence of EU1622-240, preventing us from distinguishing between these two subconductance states.

The fully open NMDAR state exhibits a substantially wider gate than those observed in the open states of other iGluRs, such as AMPA and kainate receptors[36,37] (Fig. 5b). NMDARs, including the GluN1a-2B subtype studied here, display notably higher Na^+ unitary conductance levels and Ca^{2+}/Na^+ relative permeability compared with AMPAR and kainate receptors[2,3,9,28,38–40], potentially attributable to this wider gate. Supporting this notion, the subconductance state stabilized by EU1622-14, a closely related analogue of EU1622-240 that probably stabilizes the sub-open state, has been previously shown to exhibit reduced Ca^{2+} permeability[41]. The mechanism of conductance control in NMDAR differs from that of AMPAR. AMPARs can open with as few as one glutamate bound[42] and may exhibit multiple subconductance states through conformational dynamics at the LBD[43]. Furthermore, auxiliary subunits can control conductance states[44]. By contrast, NMDAR activation requires concurrent binding of two glycine and two glutamate molecules[45], and their subconductance levels are not determined by the number of agonists. Multiple conductance levels in AMPAR have been proposed to arise from distinct arrangements of the LBD tetramer, which may cause the varying bending pattern of the M3 helices[43,46].

Physiologically, multiple conductance levels are observed in NMDARs[2,3], and the sub-open states observed in this study in the presence of the PAM could be similar to physiological sublevels. However, the PAM may also endow the observed sublevels with distinct properties that do not detectably alter the conductances measured in this study. The primary driver of channel opening is the tension generated in the GluN2B LBD-M3′ linker after glutamate binding to the GluN2B LBD, which disrupts the hydrophobic interactions at the VIVI gate (Fig. 3).

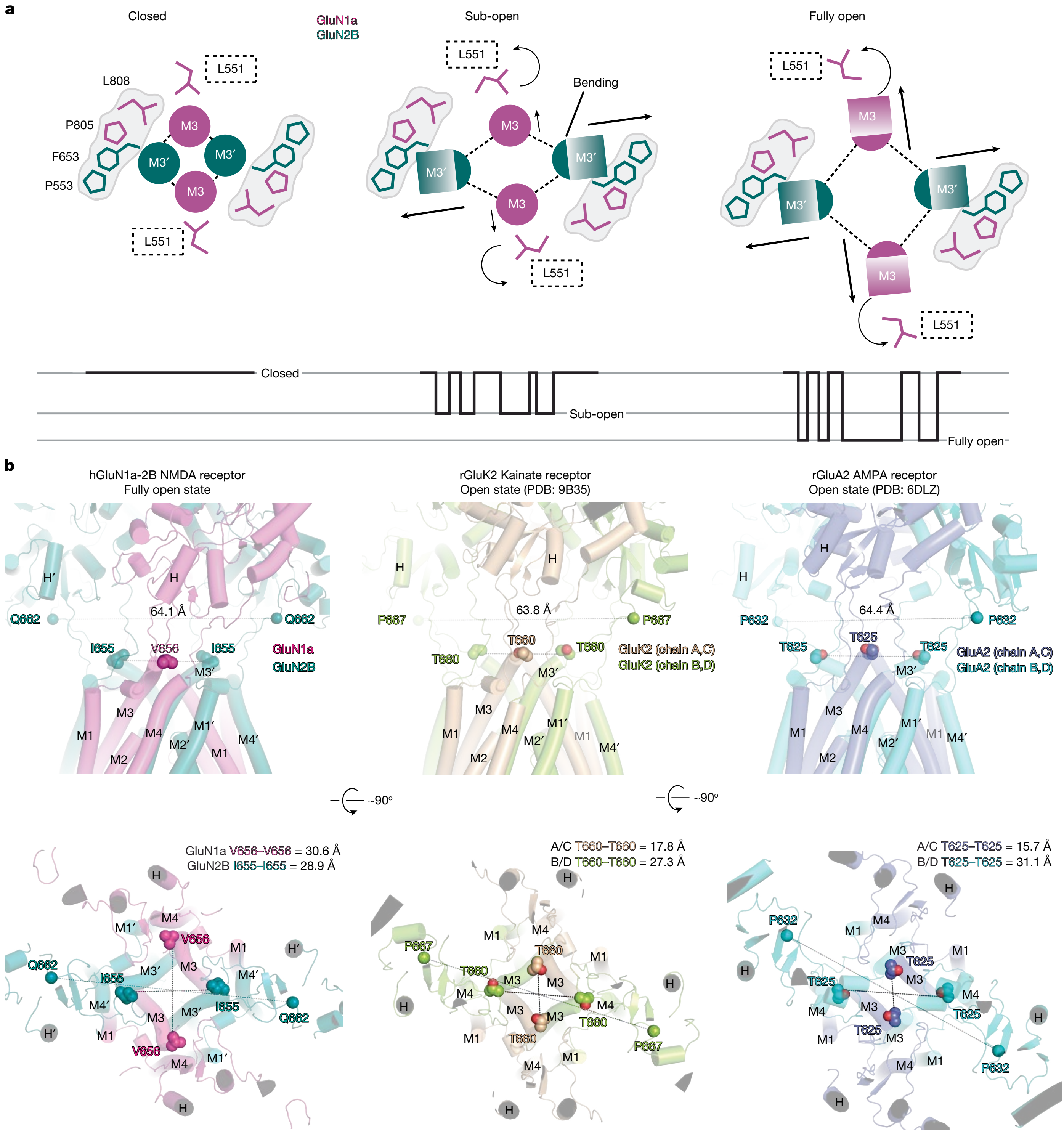

Fig. 5 | Overall mechanism and comparison with AMPAR and Kainate receptor. a, The proposed mechanism of channel pore opening and conductance level control. The closed, sub-open, and fully open states have no bending, bending in GluN2B M3′, and bending in both GluN1a M3 and GluN2B M3′, respectively. GluN1a Leu551 (pre-M1), GluN1a Leu808 and Pro805 (pre-M4), GluN2B Phe653 (M3′) and GluN2B Pro553 (pre-M1′) are networked with one another. The GluN2B M3′ bending is mediated by tension in the GluN2B LBD-M3′ loop after glutamate binding in the LBDs. This rearranges the network of the residues to substantially move the GluN1a pre-M1 loop, especially GluN1a Leu551, which is essential for accommodating GluN1a M3 bending. These conformational states are represented by a closed channel, a subconducting state and a full conducting state, respectively, at the single-channel level (bottom). **b**, Top and side views of the channel pore of NMDAR, Kainate receptor and AMPAR. The distances between GluN2B Gln662s, between GluK2 Pro667s and between GluA2 Pro632s represent the LBD-M3′ tension. The gate dimensions were measured as the distances between GluN1a Val656s (magenta) and GluN2B Ile655s (deep teal), GluK2 Thr660s (A/C subunits are shown in wheat and B/D subunits are shown in lime green) and GluA2 Thr625s (A/C subunits are shown in light purple and B/D subunits are shown in cyan).

By contrast, the GluN1a LBD-M3 linker does not generate sufficient tension to initiate GluN1a M3 bending. Instead, the bending of GluN1a M3 probably arises as a secondary effect of conformational changes initiated by GluN2B M3′ bending, particularly the movement of the GluN1a pre-M1 region (Fig. 3b and Supplementary Video 1). Thus, the sequence of channel gate opening likely proceeds with GluN2B M3′ bending, followed by GluN1a M3 bending, but not in the reverse order.

Finally, the 24S-HC-bound and PS-bound structures represent to our knowledge the first identified neurosteroid-binding sites within the iGluR family, revealing distinct binding modes and stoichiometries at the juxtamembrane pocket. Considering the functional diversity and endogenous presence of neurosteroids, the binding information identified in this study provides a strategic framework for safe therapeutic targeting of NMDAR activity.

Online content

Any methods, additional references, Nature Portfolio reporting summaries, source data, extended data, supplementary information, acknowledgements, peer review information; details of author contributions and competing interests; and statements of data and code availability are available at https://doi.org/10.1038/s41586-025-09695-4.

1. Hille, B. *Ion Channels of Excitable Membranes* 3rd edn (Sinauer, 2001).
2. Jahr, C. E. & Stevens, C. F. Glutamate activates multiple single channel conductances in hippocampal neurons. *Nature* **325**, 522–525 (1987).
3. Cull-Candy, S. G. & Usowicz, M. M. Multiple-conductance channels activated by excitatory amino acids in cerebellar neurons. *Nature* **325**, 525–528 (1987).
4. Schneggenburger, R. & Ascher, P. Coupling of permeation and gating in an NMDA-channel pore mutant. *Neuron* **18**, 167–177 (1997).
5. Banke, T. G. & Traynelis, S. F. Activation of NR1/NR2B NMDA receptors. *Nat. Neurosci.* **6**, 144–152 (2003).
6. Popescu, G. & Auerbach, A. Modal gating of NMDA receptors and the shape of their synaptic response. *Nat. Neurosci.* **6**, 476–483 (2003).
7. Bliss, T. V. P. & Collingridge, G. L. A synaptic model of memory: long-term potentiation in the hippocampus. *Nature* **361**, 31–39 (1993).
8. Malenka, R. C. & Bear, M. F. LTP and LTD: an embarrassment of riches. *Neuron* **44**, 5–21 (2004).
9. Hansen, K. B. et al. Structure, function, and pharmacology of glutamate receptor ion channels. *Pharmacol. Rev.* **73**, 298–487 (2021).
10. Karakas, E. & Furukawa, H. Crystal structure of a heterotetrameric NMDA receptor ion channel. *Science* **344**, 992–997 (2014).
11. Lee, C. H. et al. NMDA receptor structures reveal subunit arrangement and pore architecture. *Nature* **511**, 191–197 (2014).
12. Wang, J. X. & Furukawa, H. Dissecting diverse functions of NMDA receptors by structural biology. *Curr. Opin. Struct. Biol.* **54**, 34–42 (2019).
13. Mony, L. & Paoletti, P. Mechanisms of NMDA receptor regulation. *Curr. Opin. Neurobiol.* **83**, 102815 (2023).
14. Zhou, C. & Tajima, N. Structural insights into NMDA receptor pharmacology. *Biochem. Soc. Trans.* **51**, 1713–1731 (2023).
15. Wu, E., Zhang, J., Zhang, J. & Zhu, S. Structural insights into gating mechanism and allosteric regulation of NMDA receptors. *Curr. Opin. Neurobiol.* **83**, 102806 (2023).
16. Hansen, K. B. et al. Structure, function, and allosteric modulation of NMDA receptors. *J. Gen. Physiol.* **150**, 1081–1105 (2018).
17. Ratner, M. H., Kumaresan, V. & Farb, D. H. Neurosteroid actions in memory and neurologic/neuropsychiatric disorders. *Front. Endocrinol.* **10**, 169 (2019).
18. Hanson, J. E. et al. Therapeutic potential of *N*-methyl-D-aspartate receptor modulators in psychiatry. *Neuropsychopharmacology* **49**, 51–66 (2024).
19. Zorumski, C. F. et al. New directions in neurosteroid therapeutics in neuropsychiatry. *Neurosci. Biobehav. Rev.* **172**, 106119 (2025).
20. Hrcka Krausova, B. et al. Site of action of brain neurosteroid pregnenolone sulfate at the *N*-methyl-D-aspartate receptor. *J. Neurosci.* **40**, 5922 (2020).
21. Perszyk, R. E. et al. Biased modulators of NMDA receptors control channel opening and ion selectivity. *Nat. Chem. Biol.* **16**, 188–196 (2020).
22. Chou, T. H. et al. Molecular mechanism of ligand gating and opening of NMDA receptor. *Nature* **632**, 209–217 (2024).
23. Ullman, E. Z. et al. Mechanisms of action underlying conductance-modifying positive allosteric modulators of the NMDA receptor. *Mol. Pharmacol.* **106**, 334–353 (2024).
24. Paul, S. M. et al. The major brain cholesterol metabolite 24(*S*)-hydroxycholesterol is a potent allosteric modulator of *N*-methyl-D-aspartate receptors. *J. Neurosci.* **33**, 17290–17300 (2013).
25. Wu, F. S., Gibbs, T. T. & Farb, D. H. Pregnenolone sulfate: a positive allosteric modulator at the *N*-methyl-D-aspartate receptor. *Mol. Pharmacol.* **40**, 333–336 (1991).
26. Fritzemeier, R. G. et al. Thienopyrimidinone derivatives as a GluN2B/C/D biased, positive allosteric modulator of the *N*-methyl-D-aspartate receptor. *J. Med. Chem.* **68**, 9303–9322 (2025).
27. Premkumar, L. S., Qin, F. & Auerbach, A. Subconductance States of a mutant NMDA receptor channel kinetics, calcium, and voltage dependence. *J. Gen. Physiol.* **109**, 181–189 (1997).
28. Stern, P., Béhé, P., Schoepfer, R. & Colquhoun, D. Single-channel conductances of NMDA receptors expressed from cloned cDNAs: comparison with native receptors. *Proc. R. Soc. Lond. B* **250**, 271–277 (1997).
29. Banke, T. G., Dravid, S. M. & Traynelis, S. F. Protons trap NR1/NR2B NMDA receptors in a nonconducting state. *J. Neurosci.* **25**, 42–51 (2005).
30. Huang, Z. & Gibb, A. J. Mg^{2+} block properties of triheteromeric GluN1–GluN2B–GluN2D NMDA receptors on neonatal rat substantia nigra pars compacta dopaminergic neurones. *J. Physiol.* **592**, 2059–2078 (2014).
31. Kang, H. et al. Structural basis for channel gating and blockade in tri-heteromeric GluN1-2B-2D NMDA receptor. *Neuron* https://doi.org/10.1016/j.neuron.2025.01.013 (2025).
32. Chou, T. H., Tajima, N., Romero-Hernandez, A. & Furukawa, H. Structural basis of functional transitions in mammalian NMDA receptors. *Cell* **182**, 357–371 (2020).
33. Tajima, N. et al. Activation of NMDA receptors and the mechanism of inhibition by ifenprodil. *Nature* **534**, 63–68 (2016).
34. Smart, O. S., Neduvelil, J. G., Wang, X., Wallace, B. A. & Sansom, M. S. P. HOLE: a program for the analysis of the pore dimensions of ion channel structural models. *J. Mol. Graphics* **14**, 354–360 (1996).
35. Amin, J. B. et al. Two gates mediate NMDA receptor activity and are under subunit-specific regulation. *Nat. Commun.* **14**, 1623 (2023).
36. Twomey, E. C., Yelshanskaya, M. V., Grassucci, R. A., Frank, J. & Sobolevsky, A. I. Channel opening and gating mechanism in AMPA-subtype glutamate receptors. *Nature* **549**, 60–65 (2017).
37. Gangwar, S. P. et al. Kainate receptor channel opening and gating mechanism. *Nature* **630**, 762–768 (2024).
38. Swanson, G. T., Kamboj, S. K. & Cull-Candy, S. G. Single-channel properties of recombinant AMPA receptors depend on RNA editing, splice variation, and subunit composition. *J. Neurosci.* **17**, 58 (1997).
39. Zhang, W. et al. A transmembrane accessory subunit that modulates kainate-type glutamate receptors. *Neuron* **61**, 385–396 (2009).
40. Watanabe, J., Beck, C., Kuner, T., Premkumar, L. S. & Wollmuth, L. P. DRPEER: a motif in the extracellular vestibule conferring high Ca^{2+} flux rates in NMDA receptor channels. *J. Neurosci.* **22**, 10209–10216 (2002).
41. Perszyk, R. E. et al. Hodgkin-Huxley-Katz Prize Lecture: genetic and pharmacological control of glutamate receptor channel through a highly conserved gating motif. *J. Physiol.* https://doi.org/10.1113/JP278086 (2020).
42. Rosenmund, C., Stern-Bach, Y. & Stevens, C. F. The tetrameric structure of a glutamate receptor channel. *Science* **280**, 1596–1599 (1998).
43. Yelshanskaya, M. V., Patel, D. S., Kottke, C. M., Kurnikova, M. G. & Sobolevsky, A. I. Opening of glutamate receptor channel to subconductance levels. *Nature* **605**, 172–178 (2022).
44. Coombs, I. D. & Cull-Candy, S. G. Single-channel mechanisms underlying the function, diversity and plasticity of AMPA receptors. *Neuropharmacology* **198**, 108781 (2021).
45. Benveniste, M. & Mayer, M. L. Kinetic analysis of antagonist action at *N*-methyl-D-aspartic acid receptors. Two binding sites each for glutamate and glycine. *Biophys. J.* **59**, 560–573 (1991).
46. Hale, W. D., Huganir, R. L. & Twomey, E. C. Architecture, activation, and conformational plasticity in the GluA4 AMPA receptor. Preprint at *bioRxiv* https://doi.org/10.1101/2025.06.12.659357 (2025).

Methods

Purification of GluN1a-2B NMDAR

Human GluN1a-2B NMDAR proteins were expressed in the EarlyBac system[47] with slight modification. In brief, GluN2B was attached to the *Xenopus* GluN1 signal sequence and inserted into the pFP10 vector. GluN1a was inserted into the pUCp10 vector and recombined with the pFP10-GluN2B vector using Cre recombinase. This fused vector was used to make baculovirus using the Bac-to-Bac system. Sf9 cells were cultured to 4.0×10^6 cells per ml and were infected with freshly made P2 baculovirus. After 48 h of infection, cells were collected and resuspended in 20 mM HEPES 7.5 mM, 150 mM NaCl, 1 mM ethylenediaminetetraacetic acid (EDTA) and 1 mM phenylmethylsulfonyl fluoride. Cell lysis was done using Emulsiflex C3 (Avestin) and centrifuged at 40,000 rpm for 30 min at 4 °C to retrieve the membrane fraction. The collected membrane fraction was resuspended in 20 mM HEPES pH 7.5, 150 mM NaCl, 1 mM glycine, 1 mM EDTA, 0.5% lauryl maltose neopentyl glycol (LMNG), and solubilized for 2 h at 4 °C. Insoluble fractions were removed through centrifugation at 40,000 rpm for 45 min at 4 °C. The supernatant was loaded onto Strep-Tactin column, washed thoroughly and eluted with 3 mM D-desthiobiotin (Sigma-Aldrich). The eluted fractions were concentrated and loaded onto a Superose 6 10/300 column (Cytiva) equilibrated with 20 mM Tris pH 8.5, 150 mM NaCl, 1 mM glycine, 1 mM EDTA, 0.002% LMNG using the Acta Go system (Cytiva). Peak fractions containing GluN1a-2B NMDAR were collected, concentrated to around 3 mg ml^{-1}, and subjected to cryo-EM studies.

Cryo-EM sample preparation, data collection and data processing

Vitrification was done on a glow-discharged Quantifoil 1.2/1.3 Cu 200 mesh grids (EMS, for PS and 24S-HC), and Quantifoil 1.2/1.3 Cu 300 mesh + 2 nm C grids (EMS, for EU1622-240) using the FEI Vitrobot Mark 4 at 100% humidity and 8 °C. Purified fresh samples were incubated with 100 µM of 24S-HC, PS or EU1622-240 for at least 1 h at room temperature. For 24S-HC, right before vitrification, 3.5 µl of GluN1a-2B was mixed with 0.8 µl of 0.5% GDN/5 mM glutamate, loaded onto the grid and blotted for 4–6 s. For EU1622-240, right before vitrification, 3.5 µl of GluN1a-2B was mixed with 0.4 µl of 0.5% GDN/5 mM glutamate and MgCl_2, loaded onto the grid and blotted for 2.2–3 s. Videos were acquired on the Titan Krios G3 at 300 keV system coupled to the K3 BioQuantum direct image detector and a GIF energy filter using EPU v.2.10.0.5. Magnification was set to ×105,000 using a defocus range of between −2.2 µm and −0.8 µm, and the sample was exposed to a total dose of around 58 Å. All datasets were processed using Cryosparc (v.4.6.2)[48–50]. Collected videos were motion corrected and CTF-estimated and micrographs with CTF estimation lower than 5–6 Å were removed. Templates were made by processing 500 videos and picking particles using 200 Å as a particle size. The template-picked particles were extracted and binned ×4 to enhance the processing speed. Extracted particles were passed through multiple rounds of 2D classification, ab initio and heterogeneous refinement to remove junk particles and separate different classes fully. Final particle sets were re-extracted to 400 box size and refined using non-uniform refinement. To enhance the overall resolution, reference-free motion correction was done, and the particles were further refined using non-uniform refinement and local refinement. The final composite map was made with vop-maximum in ChimeraX v.1.4, combining the ATD-LBD local refined map and the TMD local refined map. Model building was initially done by fitting GluN1a-2B (Protein Data Bank (PDB): 7SAA or 9ARE)[22,51] to the cryo-EM density map using ChimeraX (v.1.4)[52]. Further processing was done using Phenix (v1.20.1-4487)[53] and manually refined using winCOOT (v.0.9.8.95)[54].

TEVC electrophysiology

We expressed WT and mutant GluN1-1a and GluN2B NMDARs in *Xenopus laevis* oocytes. Linearized DNAs were transcribed using mMessage mMachine t7 transcription kit (Invitrogen). The resulting cRNAs encoding GluN1-1a and GluN2B were injected into defolliculated *X. laevis* oocytes at a 1:1 ratio (10 ng total). Injected oocytes were maintained in ×0.5 L-15 medium supplemented with 20 mM HEPES at pH 7.5, 100× penicillin–streptomycin solution (Thermo Fisher Scientific), and 0.6% FBS for 1–2 days at 18 °C. TEVC (Axoclamp-2B) recordings were performed using an extracellular solution containing 5 mM HEPES, 100 mM NaCl, 0.3 mM BaCl_2, 10 mM tricine at final pH 7.4 (adjusted with KOH). The current was measured using an agarose-tipped microelectrode (0.4–0.9 MΩ) at the holding potential of −60 mV. Maximal response currents were evoked by 100 µM of glycine and 100 µM of L-glutamate. Data were acquired by the PatchMaster v2x32 (HEKA) and analysed using Excel and GraphPad Prism 10. For the EC_{50} measurement, the late portion of the plateau phase was used, specifically just before any signal spikes after compound removal. Nonlinear regression (agonist versus response) was performed using equation (1), where Y is the measured effect, X is ligand concentration and n is Hill slope.

$$Y = \text{Basal\_response} + \frac{(\text{Maximum\_response} - \text{Basal\_response})}{X^n + \text{EC}_{50}{}^n} \tag{1}$$

All concentration points were measured within a single oocyte; six independent oocytes were used for 24S-HC and, for PS, two different sets of concentration points (0 µM, 0.2 µM, 2 µM, 10 µM, 25 µM, 50 µM, 100 µM, 200 µM) or (0 µM, 1 µM, 10 µM, 30 µM, 60 µM, 150 µM, 250 µM) were measured with 12 independent oocytes. For the mutant data, one-way ANOVA was used followed by Dunnett's test (two-sided) comparing each group to WT. P values were adjusted for multiple comparisons with family-wise $\alpha = 0.05$.

Single-channel recording and analysis

Single-channel recordings were made from human embryonic kidney (HEK293T, CRL 3216, ATCC) cells cultured in Dulbecco's modified Eagle's medium (Thermo Fisher Scientific, 10566016) and supplemented with 10% FBS (R&D Systems, S12850), 10 µg ml^{-1} streptomycin and 10 U ml^{-1} penicillin, maintained in a 37 °C incubator with 5% CO_2. Then, 24–48 h before patch-clamp recordings, cells were plated onto poly-D-lysine-coated glass coverslips (0.1 mg ml^{-1}, Sigma-Aldrich, P7280). Cells were transiently transfected with cDNA encoding GluN1–GluN2B–GFP using the calcium phosphate method in a 24-well plate with 500 ng of cDNA at a ratio of 1:1:1 (GluN1:GluN2B:eGFP). Then, 4–6 h after transfection, the medium was replaced and supplemented with 200 µM D,L-APV and 200 µM 7-chlorokynurenic acid to reduce NMDA receptor-mediated cytotoxicity. Patch pipettes were pulled on a Sutter P-1000 from aluminosilicate (1.5 mm (outer diameter) × 1 mm (inner diameter); Sutter Instruments) and had a resistance of 7 to 16 MΩ. The external bath solution contained 150 mM NaCl, 3 mM KCl, 10 mM HEPES, 5 mM mannitol, 0.01 mM EDTA and 0.5 mM CaCl_2. The pipette internal solution contained 110 mM D-gluconate, 110 mM CsOH, 30 mM CsCl, 5 mM BAPTA, 5 mM HEPES, 4 mM NaCl, 2 mM MgCl_2, 2 mM Na-ATP, 0.5 mM CaCl_2, 0.3 mM Na-GTP (pH 7.35). Outside-out patches excised from HEK293T were held under voltage clamp at −80 mV using a Warner Patch Clamp PC-505B amplifier (Warner Instruments). Current responses were filtered at 10 kHz (−3 dB, Bessel) and digitized at 50 kHz using a Digidata 1440 A and Clampex 10.7 (Molecular Devices). Test solutions were applied using a gravity-fed dual barrel theta tube (Siskiyou Corporation). Solutions contained 100 µM glutamate and 100 µM glycine (plus 0.1–0.25% DMSO and 0.01% cremophor EL) with or without 10 µM 24S-HC and/or 150 µM PS. All recordings were made at room temperature (23 °C). Single-channel current recordings were filtered off-line at 1 kHz (−3 dB, Gaussian filter[23]), and single-channel openings were idealized using a custom threshold crossing algorithm to detect openings that reached 30% of full amplitude and closings that dropped to 70% of a given open level[23]. To obtain the dwell time of open and closed events, we calculated the exact time at which the opening reached 50% of the fitted amplitude by interpolation from the datapoints defining the transitions for each open and closed period. We then corrected the duration of brief open and closed periods by determining the change in duration of simulated square steps of various durations due to filtering. Changes of more than 1.5 pA were considered to be a real difference between events for open durations; direct transitions that changed amplitude less than 1.5 pA were concatenated and were marked as a single open period. The open resolution was 50 µs, and openings that were briefer than this were concatenated to the adjacent preceding dwell time (open or closed). Closures that were briefer than the 50 µs resolution were added to the sum of the two adjacent open segments. The maximum-likelihood method was used to fit the open duration histograms with the sum of two or three exponential functions. The amplitude histograms were made from the mean amplitudes of datapoints that were longer than 2.5 filter rise times and more negative than −1 pA, to ensure amplitudes reached 99.8% of the maximum value and that we did not include baseline noise. For sublevel analysis, changes of more than 0.5 pA between open amplitudes were considered a real difference. The amplitude histograms were fitted using the maximum-likelihood method with the sum of two Gaussian components. We did not correct for the estimated junction potential, and report chord conductance values assuming the reversal potential is 0 mV. To estimate the channel open probability (nP_o), we divided the integral (Q) of the baseline-corrected recording by the product of the mean channel amplitude (i) and the recording duration (time) to obtain the product of the estimated number of channels (n) and the open probability (P_o):

$$\frac{Q}{i \times \text{time}} = n \times P_o. \tag{2}$$

Conductance levels were determined for neurosteroids for patches that showed unambiguous enhancement of open probability, to remove the potential confound of channel rundown, and to ensure that the lack of an effect on conductance was not a result of the lack of effect of the neurosteroid.

Measurement of Ca^{2+} permeability

The current–voltage relationship was determined from HEK cells expressing GluN1/GluN2B by applying a voltage-step protocol, which began from a holding potential of −60 mV then increased by 5 mV every 250 ms until it reached +30 mV. Receptor responses were measured in the presence 100 µM glutamate and 30 µM glycine, and the seal leak current–voltage curve obtained in the absence of agonist subtracted. Cells were patched in a bath solution containing 1 mM Ca^{2+} and the low Ca^{2+} test solution contained 0.1 mM Ca^{2+} and the high Ca^{2+} test solution contained 10 mM Ca^{2+}. The current–voltage relationship was calculated in the presence of vehicle (DMSO) or EU1622-240 (3 µM). A sub-saturating concentration of EU1622-240 was used to attempt to limit excessive receptor response amplitudes. Only current responses of <3,000 pA were analysed, and recordings were omitted from cells where the leak current in the absence of agonist was more than 100% of the response to agonist, and if the leak current in 10 mM Ca^{2+} was more than twofold greater than the leak in 0.1 mM Ca^{2+}. All solutions contained a constant $[Na^+]$, but varied $[Ca^{2+}]$. The patch pipette was first placed in our standard recording (bath) solution that contained 150mM NaCl, 3 mM KCl, 1 mM $CaCl_2$, 10 mM HEPES (adjusted to pH 7.2 with NaOH). To mitigate any variations of junction potential at the ground pellet, we used a 3 M KCl agar bridge, which was replaced multiple times per recording day (replaced every 2 h). The pipette internal solution contained 140 mM KCl, 10 mM M-BAPTA, 10 mM HEPES (adjusted to pH 7.2 with NaOH). We determined the reversal potential for each curve by fitting a fourth-order polynomial function to the current–voltage relationship. All voltages reported were corrected for junction potential (all base solutions matched those used previously[21] and were therefore corrected by the same calculated liquid junction potentials reported). The external patching solution had a +6.6 mV, the low Ca^{2+} had a −0.1 mV and high-Ca^{2+} solutions had a +1.1 mV junction potential referenced to the pipette solution. The relative calcium permeability (Ca^{2+} to monovalent cations) was calculated as previously reported (high monovalent method)[21]. We used a modified version of the Lewis equation[55] and our experimentally determined reversal potentials to calculate the relative permeability of Ca^{2+} to Na^+, as described in equations (3) and (4) below and in refs. 21,56, where R is the ideal gas constant (joules per kelvin per mole), F is the Faraday constant (coulombs per mole) and T is the temperature in kelvin.

$$V_{\text{rev,Ca}} - V_{\text{rev,Na}} = \Delta V_{\text{rev}} = \frac{RT}{F} \ln\left(1 + \frac{4\frac{P_{\text{Ca}}}{P_{\text{Na}}}[\text{Ca}^{2+}]_o}{[\text{Na}^+]_o\left[1 + \exp\left(\frac{V_{\text{rev,Ca}}}{RT/F}\right)\right]}\right) \tag{3}$$

$$\frac{P_{\text{Ca}}}{P_{\text{Na}}} = \frac{\left[\exp\left(\Delta V_{\text{rev}}\frac{F}{RT}\right) - 1\right][\text{Na}^+]_o\left[1 + \exp\left(\frac{V_{\text{rev,Ca}}}{RT/F}\right)\right]}{4[\text{Ca}^{2+}]_o} \tag{4}$$

Molecular dynamics simulation

Cryo-EM structures were refined before simulation by adding missing atoms with MODELLER (v.9.12)[57], with only the TMDs retained to facilitate sampling. The free-energy profile was obtained using umbrella sampling combined with the GROMACS weighted histogram analysis method (WHAM). For each umbrella window, the starting configuration was prepared by initially positioning the monovalent ion at the centre of geometry of the Asn-ring Cα atoms. The ion was then shifted stepwise by 0.5 Å along the pore's z axis (perpendicular to the membrane plane), extending into bulk water on both extracellular and intracellular sides to ensure adequate sampling. Each configuration underwent steepest-descent minimization until convergence, with harmonic restraints of 1,000 kJ mol^{-1} nm^{-2} applied to protein heavy atoms and 10,000 kJ mol^{-1} nm^{-2} to the ion. After minimization, systems were equilibrated for 2 ns in the isothermal–isobaric ensemble (NPT ensemble) under umbrella restraints. Most windows used a restraint of 1,000 kJ mol^{-1} nm^{-2}, although those located near steep barriers or saddle points employed stronger restraints of 2,000–3,000 kJ mol^{-1} nm^{-2}. For the open state Na^+ system, 150 umbrella windows of 14 ns each were collected, yielding a cumulative sampling time of 2.1 µs. Molecular interactions were modelled with the AMBER ff99sb-ildn protein force field[58], with Joung–Cheatham ion parameters for ions[59]. Fixed-charge force fields are suitable for monovalent ions, as they are less likely to induce polarization of surrounding residues, obviating the need for expensive polarizable force fields. Explicit water is essential for ion hydration and dehydration and, therefore, TIP3P water was chosen[60], striking a balance between speed and accuracy. AMBER Slipids parameters were selected for POPC. The system contained 150 mM NaCl plus additional counter ions to neutralize the charge. Each system contained a total of 116,567 atoms, including 25,296 water molecules and 237 POPC molecules, with initial box dimensions of 10.63 nm × 9.6 nm × 11.14 nm. Long-range electrostatics were computed using the particle mesh Ewald approach[61] and bond constraints involving hydrogen atoms were enforced with LINCS[62]. A 2 fs integration timestep was used. Temperature was regulated at 298 K with the Nosé–Hoover thermostat ($\tau_T = 0.5$ ps)[63]. Pressure was held at 1 bar using the Parrinello–Rahman barostat (semi-isotropic, compressibility 4.5×10^{-5} bar^{-1}, $\tau_P = 1$ ps). The protein Cα atoms were harmonically restrained with a force constant of 1,000 kJ mol^{-1} nm^{-2}. All simulations were performed with GROMACS (v.2021)[64]. PMFs were reconstructed using the built-in WHAM implementation. Statistical deviation estimates were derived from 200 rounds of bootstrap resampling. Convergence was monitored by block averaging: successive WHAM calculations were repeated with data extended in 2 ns increments, and PMFs were considered to be converged once differences between profiles were within the thermal energy. The reliability and reproducibility checklist for MD simulations is provided in Supplementary Table 4.

Reporting summary

Further information on research design is available in the Nature Portfolio Reporting Summary linked to this article.

Data availability

Cryo-EM data have been deposited to the PDB and Electron Microscopy Data Bank (EMDB): non-active-state Gly, Glu, PS-bound hGluN1a-2B NMDAR (PDB: 9OOS; EMDB: EMD-70671), pre-active-state Gly, Glu, PS-bound hGluN1a-2B NMDAR (PDB: 9OOT; EMDB: EMD-70672), closed-state Gly, Glu, 24S-HC-bound hGluN1a-2B NMDAR (PDB: 9OOQ; EMDB: EMD-70669), open-state Gly, Glu, 24S-HC-bound hGluN1a-2B NMDAR (PDB: 9OOR; EMDB: EMD-70671) and sub-open-state Gly, Glu, EU1622-240-bound rGluN1a-2B NMDAR (PDB: 9OOU; EMDB: EMD-70673). Source data are provided with this paper.

47. Furukawa, H., Simorowski, N. & Michalski, K. Effective production of oligomeric membrane proteins by EarlyBac-insect cell system. *Methods Enzymol.* **653**, 3–19 (2021).
48. Punjani, A., Rubinstein, J. L., Fleet, D. J. & Brubaker, M. A. cryoSPARC: algorithms for rapid unsupervised cryo-EM structure determination. *Nat. Methods* **14**, 290–296 (2017).
49. Rubinstein, J. L. & Brubaker, M. A. Alignment of cryo-EM movies of individual particles by optimization of image translations. *J. Struct. Biol.* **192**, 188–195 (2015).
50. Punjani, A., Zhang, H. & Fleet, D. J. Non-uniform refinement: adaptive regularization improves single-particle cryo-EM reconstruction. *Nat. Methods* **17**, 1214–1221 (2020).
51. Chou, T. H. et al. Structural insights into binding of therapeutic channel blockers in NMDA receptors. *Nat. Struct. Mol. Biol.* **29**, 507–518 (2022).
52. Meng, E. C. et al. UCSF ChimeraX: tools for structure building and analysis. *Protein Sci.* **32**, e4792 (2023).
53. Liebschner, D. et al. Macromolecular structure determination using X-rays, neutrons and electrons: recent developments in Phenix. *Acta Crystallogr. D* **75**, 861–877 (2019).
54. Emsley, P., Lohkamp, B., Scott, W. G. & Cowtan, K. Features and development of Coot. *Acta Crystallogr. D* **66**, 486–501 (2010).
55. Lewis, C. A. Ion-concentration dependence of the reversal potential and the single channel conductance of ion channels at the frog neuromuscular junction. *J. Physiol.* **286**, 417–445 (1979).
56. Jatzke, C., Hernandez, M. & Wollmuth, L. P. Extracellular vestibule determinants of Ca^{2+} influx in Ca^{2+}-permeable AMPA receptor channels. *J. Physiol.* **549**, 439–452 (2003).
57. Webb, B. & Sali, A. Comparative protein structure modeling using MODELLER. *Curr. Protoc. Bioinform.* **2016**, 5.6.1–5.6.37 (2016).
58. Lindorff-Larsen, K. et al. Improved side-chain torsion potentials for the Amber ff99SB protein force field. *Proteins* **78**, 1950–1958 (2010).
59. Joung, I. S. & Cheatham, T. E. III Determination of alkali and halide monovalent ion parameters for use in explicitly solvated biomolecular simulations. *J. Phys. Chem. B* **112**, 9020–9041 (2008).
60. Jorgensen, W. L., Chandrasekhar, J., Madura, J. D., Impey, R. W. & Klein, M. L. Comparison of simple potential functions for simulating liquid water. *J. Chem. Phys.* **79**, 926–935 (1983).
61. Darden, T., York, D. & Pedersen, L. Particle mesh Ewald: an N·log(N) method for Ewald sums in large systems. *J. Chem. Phys.* **98**, 10089–10092 (1993).
62. Hess, B., Bekker, H., Berendsen, H. J. C. & Fraaije, J. G. E. M. LINCS: a linear constraint solver for molecular simulations. *J. Comput. Chem.* **18**, 1463–1472 (1997).
63. Nosé, S. A unified formulation of the constant temperature molecular dynamics methods. *J. Chem. Phys.* **81**, 511–519 (1984).
64. Abraham, M. J. et al. GROMACS: high performance molecular simulations through multi-level parallelism from laptops to supercomputers. *SoftwareX* **1–2**, 19–25 (2015).

Acknowledgements We thank N. Simorowski and J. Zhang for technical support; R. Perszyk for helpful discussions; and D. Thomas and M. Wang for managing the cryo-EM facility and computing facility at Cold Spring Harbor Laboratory, respectively. This work was funded by the NIH (NS111745 and MH085926 to H.F., NS111619 to S.F.T.), Austin's purpose (H.F. and S.F.T.), Robertson funds at CSHL, Doug Fox Alzheimer's fund, Heartfelt Wing Alzheimer's fund and the Gertrude and Louis Feil Family Trust (all to H.F.). The computational work was performed with assistance from an NIH grant (S10OD028632-01).

Author contributions H.K. and H.F. conceived the project. H.K. and R.S. obtained cryo-EM structures. H.K. conducted TEVC electrophysiology experiments. E.Z.U. and S.F.T. conducted single-channel recordings. M.E. conducted molecular dynamics simulations. S.P. and D.C.L. synthesized EU1622-240. H.K. and H.F. wrote the manuscript with input from all of the authors.

Competing interests S.F.T. and H.F. are members of the medical advisory boards for the CureGRIN Foundation. S.F.T. is an advisory board member for the GRIN2B Foundation; a member of the scientific advisory boards for Eumentis Therapeutics and Neurocrine; a consultant for GRIN Therapeutics and Seyltx; a co-founder of NeurOp and AgriThera; and is on the Board of Directors for NeurOp. D.C.L. is on the Board of Directors for NeurOp. Several authors (S.P., S.F.T. and D.C.L.) are co-inventors on Emory-owned IP involving NMDA receptor modulators. The other authors declare no competing interests.

Additional information

Supplementary information The online version contains supplementary material available at https://doi.org/10.1038/s41586-025-09695-4.

Correspondence and requests for materials should be addressed to Hiro Furukawa.

Peer review information *Nature* thanks the anonymous reviewers for their contribution to the peer review of this work. Peer reviewer reports are available.

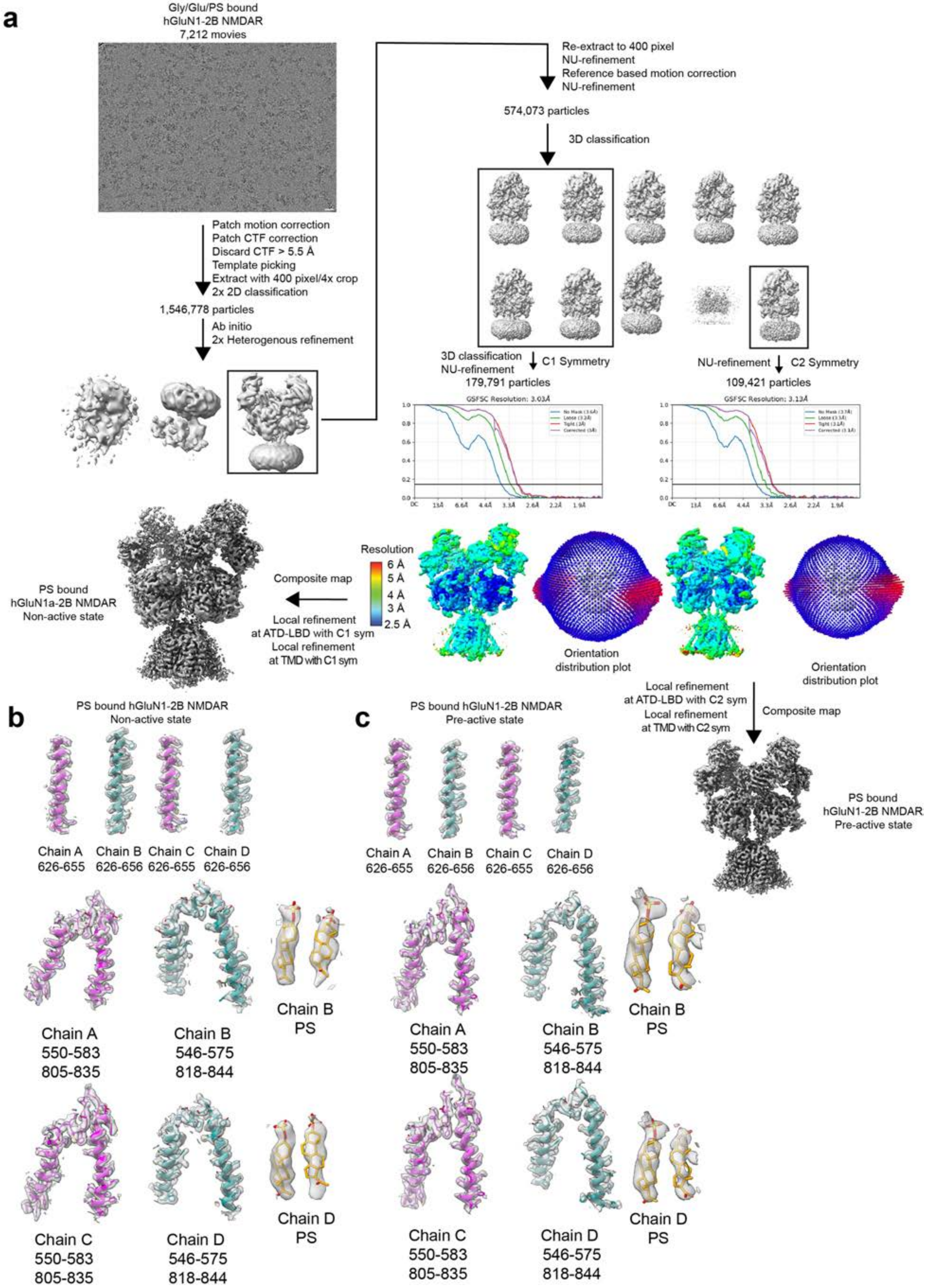

Extended Data Fig. 1 | Cryo-EM workflow for PS-bound GluN1a-2B NMDAR structures. a, Single-particle cryo-EM analysis of the glycine, glutamate, and PS-bound GluN1a-2B NMDAR. In this dataset, non-active and pre-active states were identified. Data processing was performed on sets of movies listed in Supplementary Table 2. The white bar in the micrograph indicates 20 nm. **b-c**, Map quality assessment of non-active state (b) and pre-active state (c).

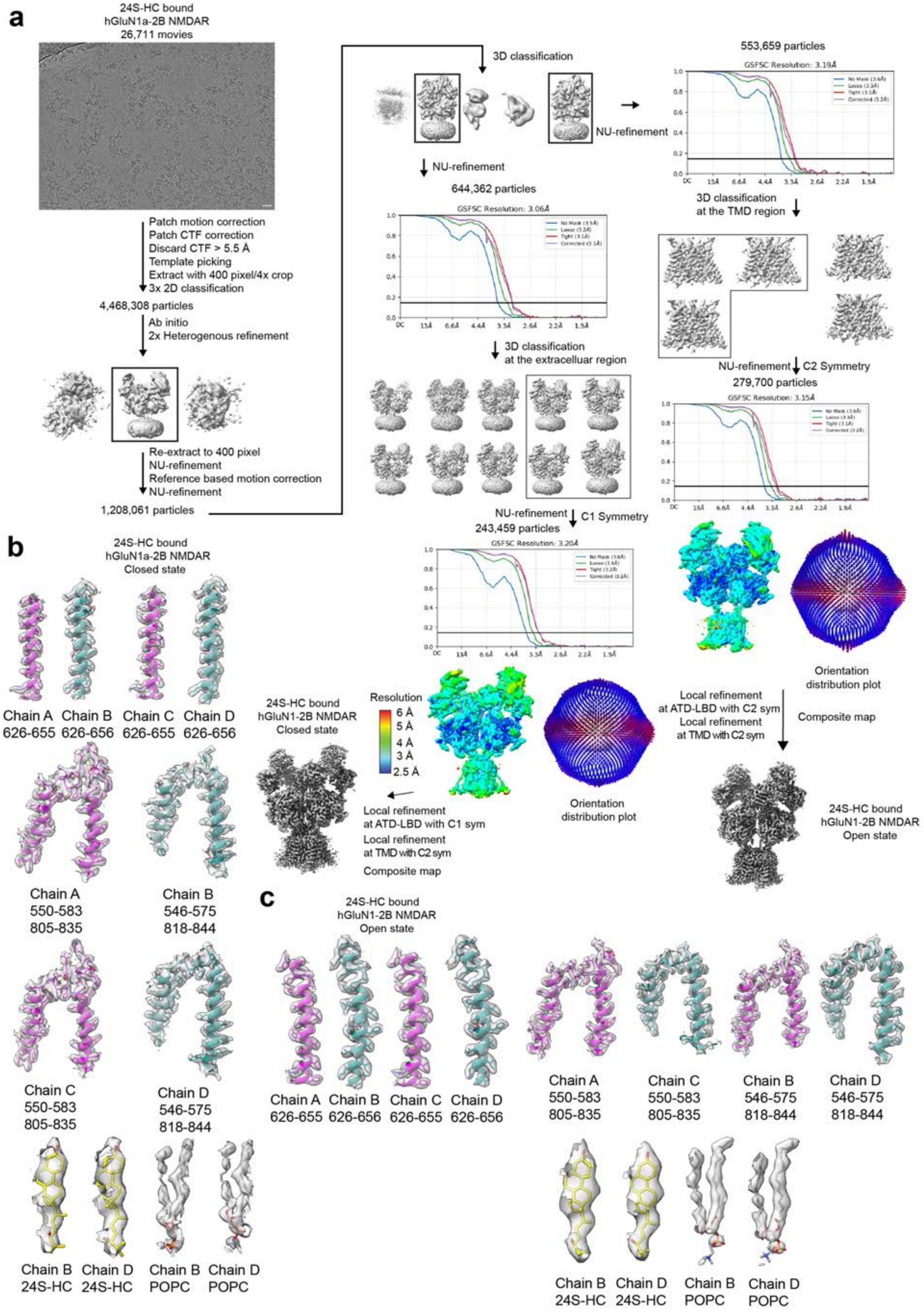

Extended Data Fig. 2 | See next page for caption.

Extended Data Fig. 2 | Cryo-EM workflow for 24S-HC-bound GluN1a-2B NMDAR structures. a, Single-particle cryo-EM analysis of the glycine, glutamate, and 24S-HC-bound GluN1a-2B NMDAR. In this dataset, the closed and open states were identified. Data processing was performed on sets of movies listed in Supplementary Table 2. The white bar in the micrograph indicates 20 nm. **b-c**, Map quality assessment of closed state (b) and open state (c).

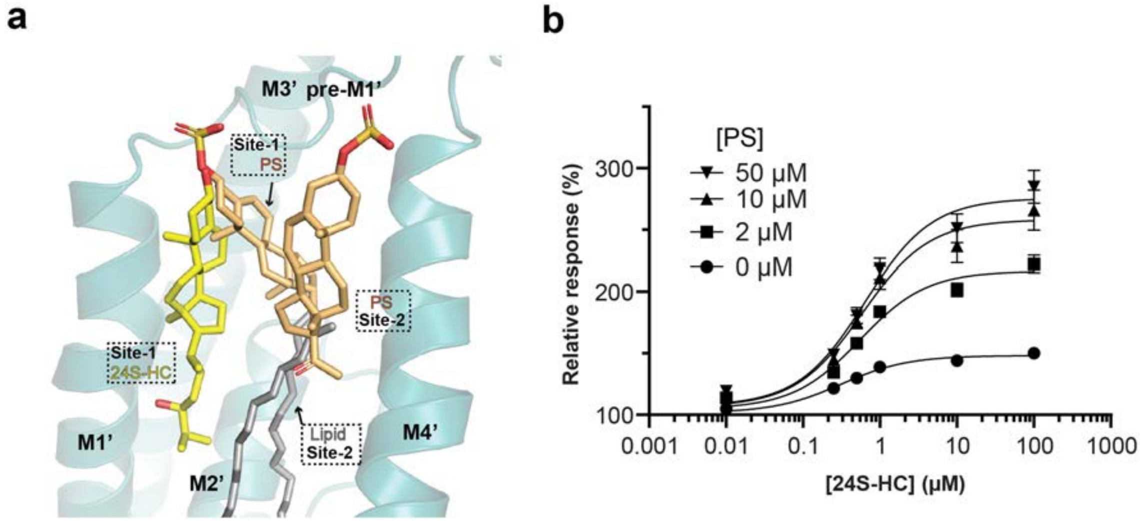

Extended Data Fig. 3 | Additive potentiating effects of PS and 24S-HC. **a**, Superposition of the PS (light orange) and 24S-HC (yellow) binding sites demonstrating distinct binding modes. At Site-1, the hydroxyl group at the tip of 24S-HC and the sulfate group of PS reside in a similar area surrounded by GluN2B pre-M1' and M1'. 24S-HC binds parallel to GluN2B M1' helix, while PS wedges into the GluN2B M2' and M3' helices. At Site-2, the ketone group of PS overlaps with the phospholipid acyl group (grey). **b**, Concentration-responses of 24S-HC in the presence of various concentrations of PS. For each PS concentration, EC_{50} values with 95% CI were 531 nM (([411 nM, 941 nM], 2 μM PS), 568 nM (([383 nM, 2.2 μM], 10 μM PS), 714 nM (([444 nM, 2.25 μM], 50 μM PS). The Hillslope was 1.19 for 2 μM, 1.14 for 10 μM, and 0.768 for 50 μM. Experiments were done with six or seven individual oocytes per PS concentration. Data for 0 μM PS condition were previously shown in Fig. 2d. Error bars indicate mean ± SEM.

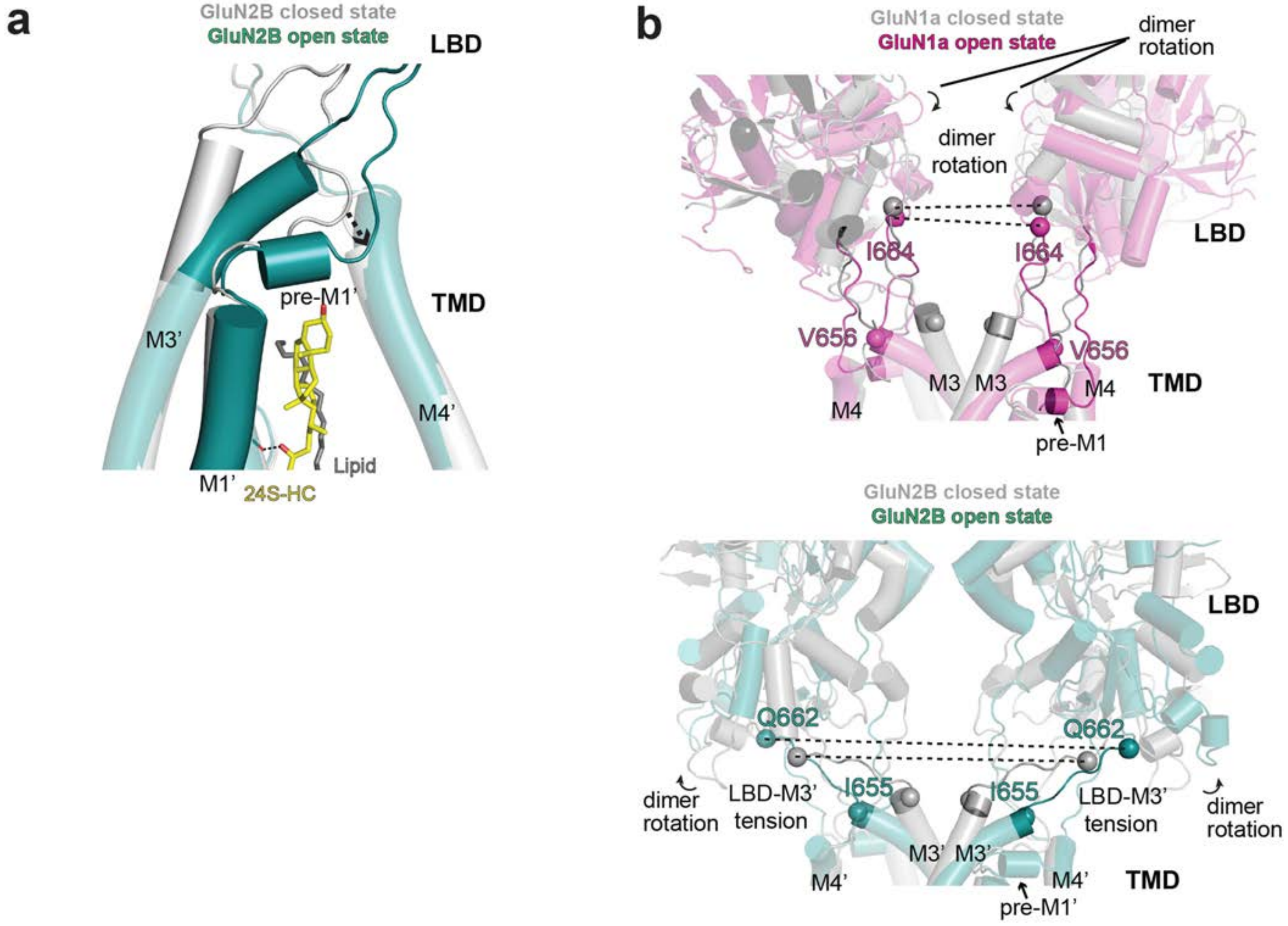

Extended Data Fig. 4 | Mechanism of 24S-HC potentiation. a, Superposition of the 24S-HC stabilized open (deep teal) and closed (grey) structures. Binding of 24S-HC at the GluN2B juxtamembrane pocket favours movement of GluN2B pre-M1' (dotted arrow). This pre-M1' movement is essential to accommodate the bending of the pore-forming GluN2B M3' helices. **b**, Conformational coupling of LBDs and TMDs in GluN1 (upper panel) and GluN2B (lower panel). Shown here are the superpositions of the closed (grey) and open (magenta and deep teal) states. The Cα atoms of the gating ring residues, right above the channel gate, for GluN1a (Ile664) and GluN2B (Gln662), are shown as spheres. Note the substantial positional shift of GluN2B Gln662 residues between open and closed states, contrasted with the minimal displacement of GluN1a Ile664 residues (dotted lines).

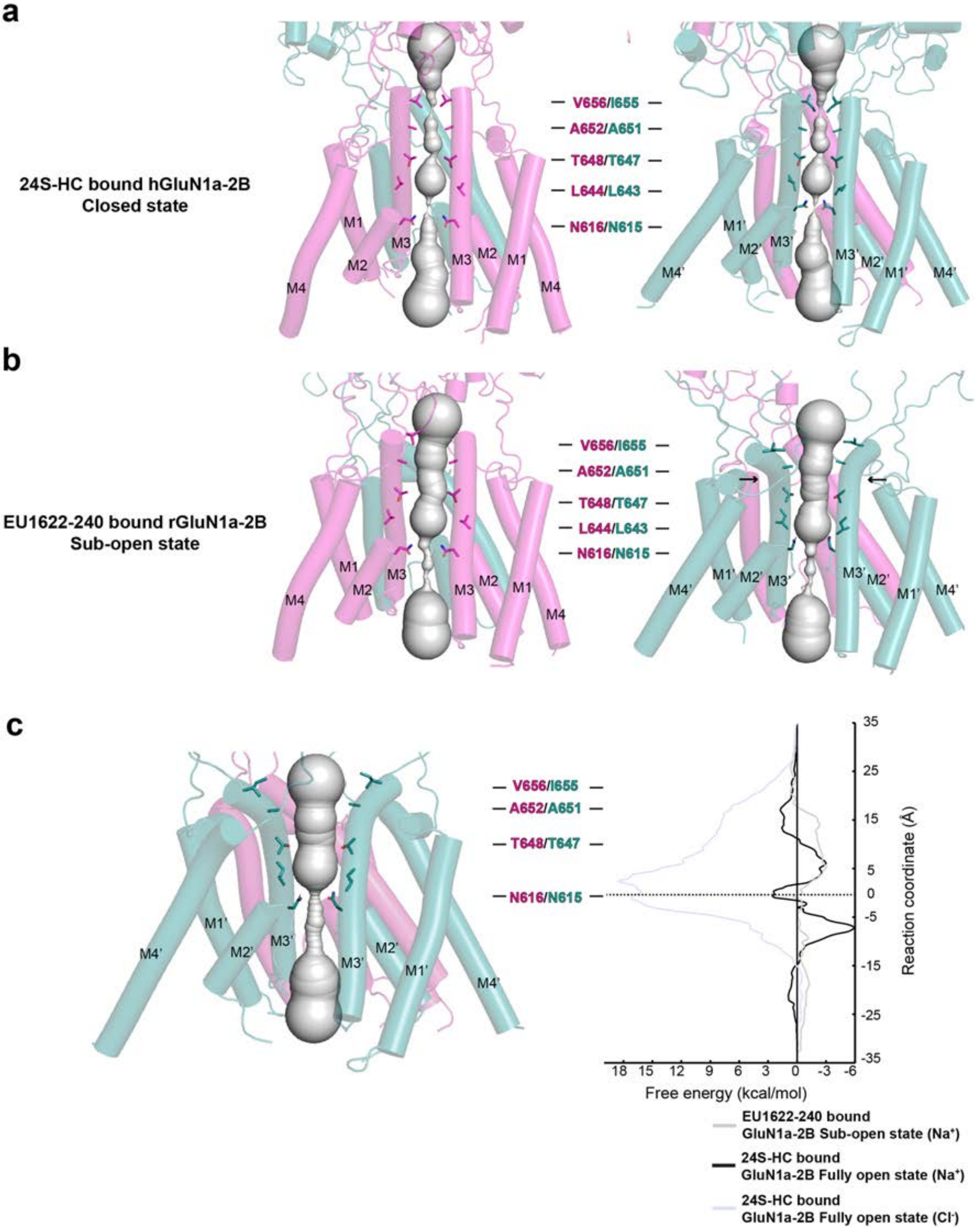

Extended Data Fig. 5 | HOLE analysis of 24S-HC-bound GluN1a-2B NMDAR in closed state and EU1622-240-bound GluN1a-2B NMDAR in sub-open state, and PMF calculation of 24S-HC-bound GluN1a-2B NMDAR in fully open state. **a**, In the closed state, the channel is highly constricted at both VIVI-gate and the Asn-ring. **b**, In the sub-open state, the channel is dilated at the VIVI-gate, with partial dilation at the Asn-ring. Arrows on the model represent the kinked region of the GluN2B M3′ helices. **c**, All-atom potential of mean force (PMF) calculation of the free energy for Na^+ ions around the TMD region of the 24S-HC-bound fully open state. The wider pore radius at the Thr-ring in the fully open state (2.2 Å in the sub-open state, 3.0 Å in the fully open state) corresponds to a modest energy barrier (~ 1.7 kcal mol^{-1}) that permits Na^+ permeation without stable binding, whereas the Asn-ring displays favourable free energy consistent with its role as a secondary gate. PMF calculation of EU1622-240-bound GluN1a-2B was adapted from ref. 21.

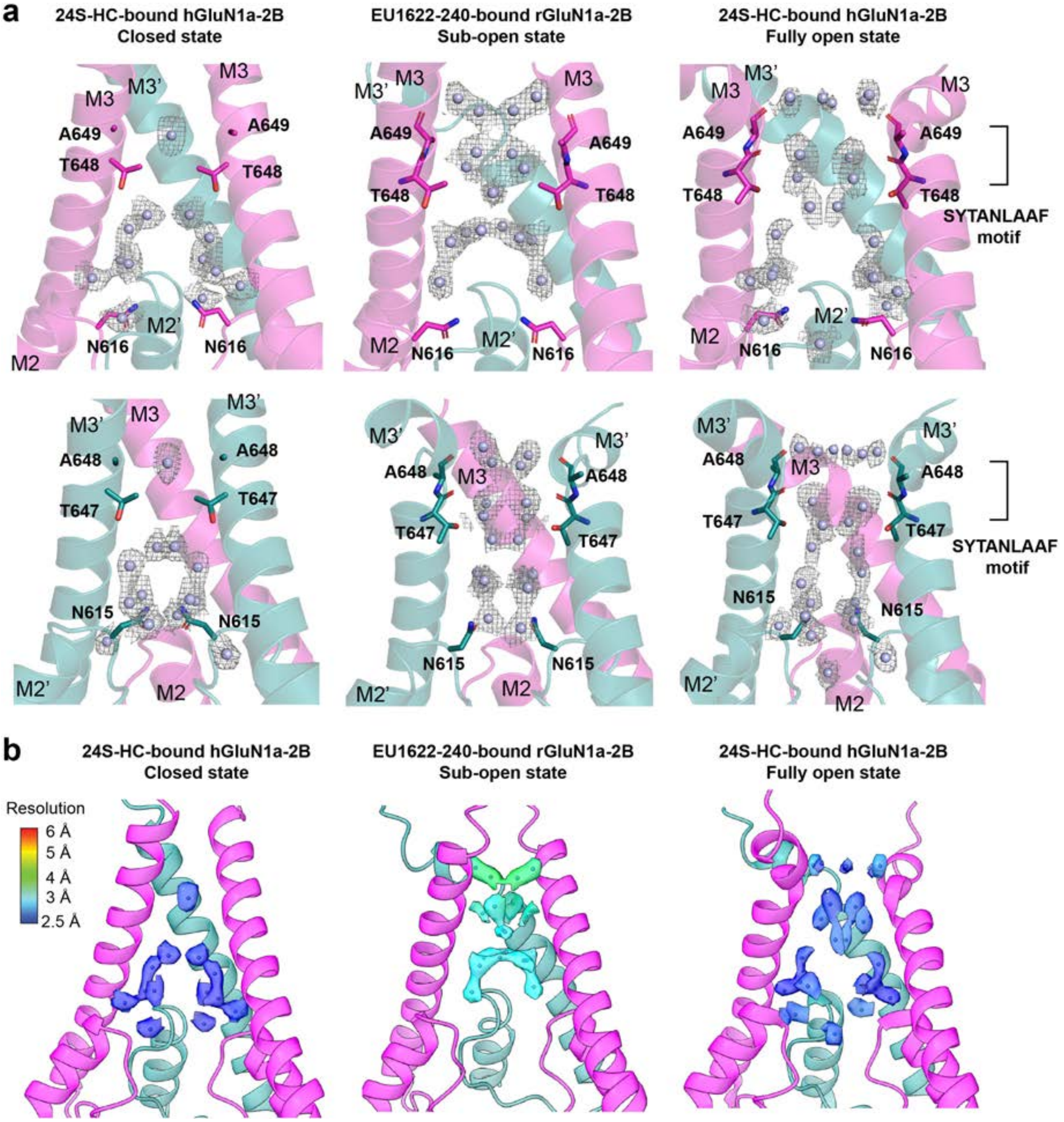

Extended Data Fig. 6 | Hydration pattern of the channel pore in closed, sub-open, and fully open states. a, Cross-section of the channel pore of the closed (left), sub-open (middle), and fully open (right) states of GluN1a-2B NMDAR. Water molecules are coloured in slate spheres overlaid with cryo-EM density in grey mesh. Key residues involved in the water network are shown. **b**, Local resolution of water density in the channel pore.

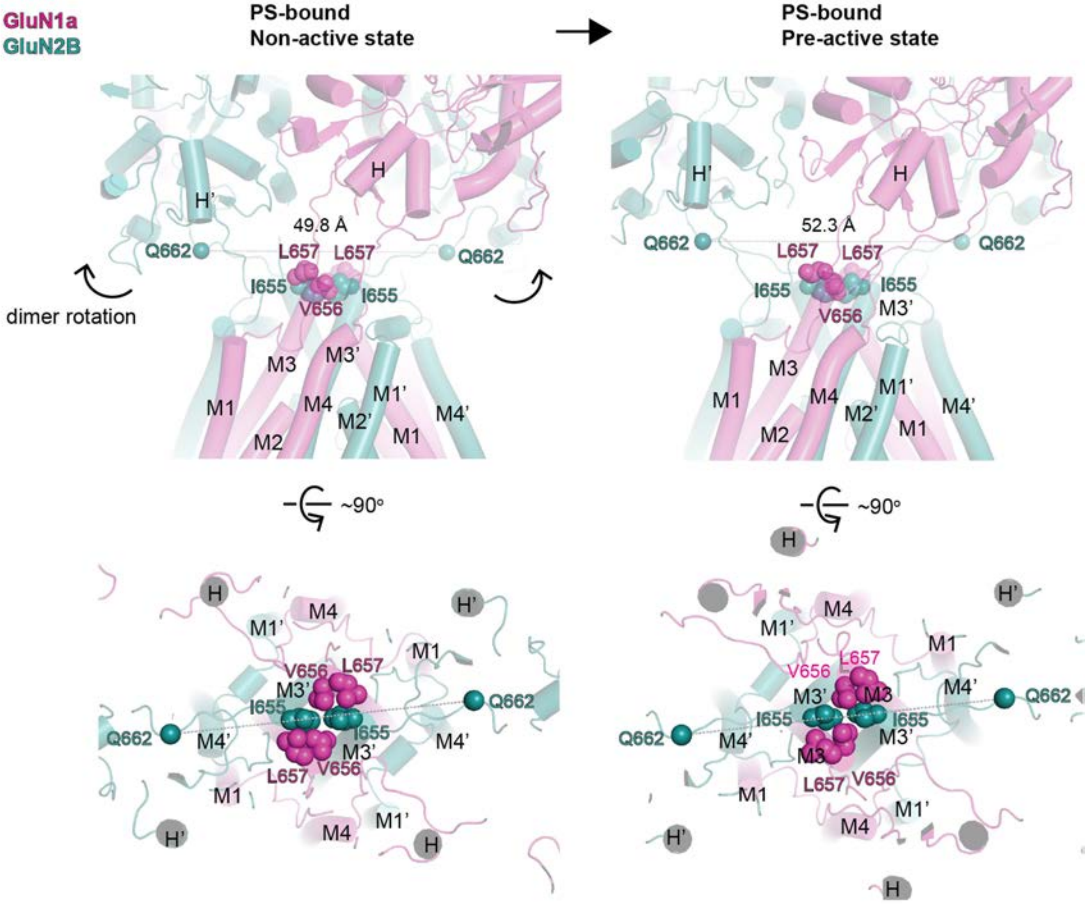

Extended Data Fig. 7 | Conformational states of the PS-bound GluN1a-2B NMDAR. The structure of the PS-bound structures in the non-active and pre-active states viewed from the side (upper panels) and top (lower panels) of the TMDs. The pre-active state shows a greater distance between the GluN2B Gln662 residues compared to the non-active state due to the GluN1a-2B LBD dimer rotations (curved arrows). In both cases, the channel gate remains closed. The hydrophobic gate residues are shown as magenta (GluN1) and deep teal (GluN2B) spheres.

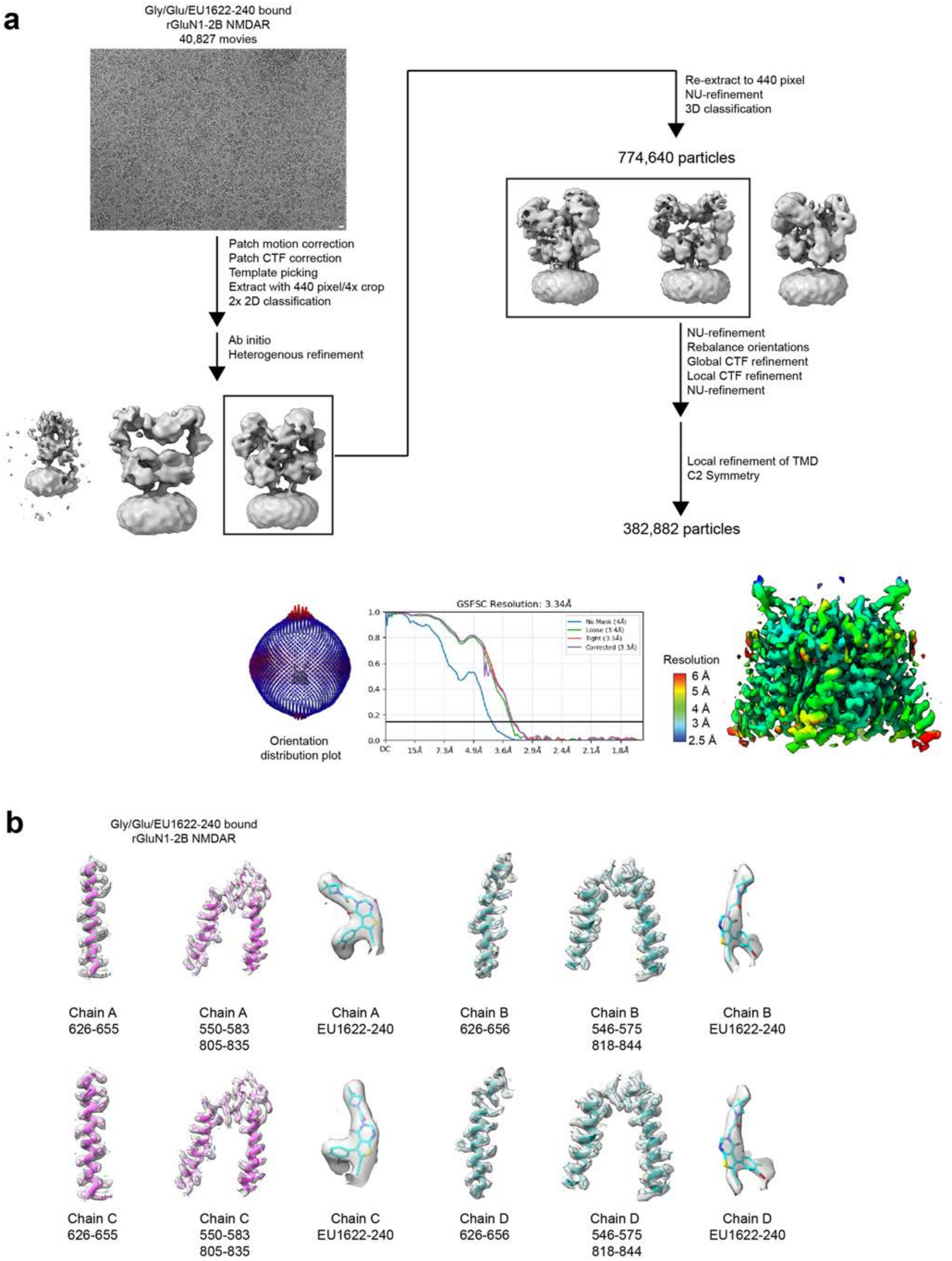

Extended Data Fig. 8 | Cryo-EM workflow for EU1622-240-bound GluN1a-2B NMDAR structure. a, Single-particle cryo-EM analysis of glycine, glutamate, and EU1622-240-bound GluN1a-2B NMDAR. The most predominant conformation of this dataset was the sub-open state. Data processing was performed on sets of movies listed in Supplementary Table 2. The white bar in the micrograph indicates 20 nm. **b**, Map quality assessment of the sub-open state.

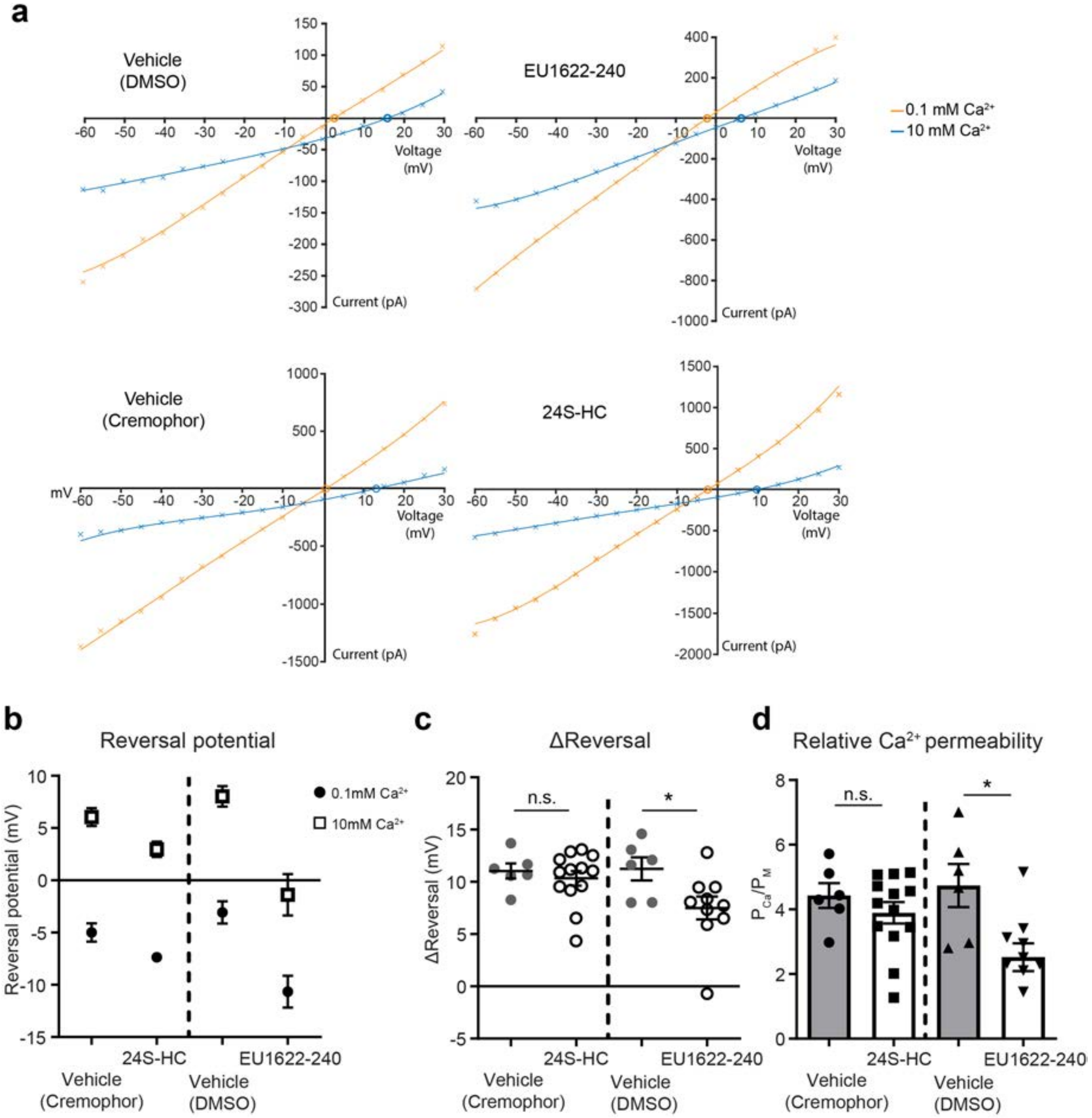

Extended Data Fig. 9 | EU1622-240 reduces Ca^{2+} permeability. **a**, The representative current-voltage curves for GluN1-2B responses in the presence 100 µM glutamate and 30 µM glycine with either vehicle (left) or 24S-HC/EU1622-240 (right) in different calcium concentrations. **b**, The average reversal potentials for vehicle and 24S-HC/EU1622-240 were determined from current-voltage relationships in solutions with different concentrations of Ca^{2+}. **c**, Mean ΔReversal potential (high Ca^{2+} minus low Ca^{2+}). Statistical significance was assessed using a two-tailed t-test; the asterisk (*) indicates p = 0.0405, n.s., not significant. **d**, The average permeability ratio of Ca^{2+} to monovalent cations derived from a modified version of Lewis equation. Values are shown as mean ± S.E.M. Data are from independent measurements: vehicles (n = 6), 24S-HC (n = 13), EU1622-240 (n = 10). Statistical significance was assessed using a two-tailed t-test; the asterisk (*) indicates p = 0.0112, n.s., not significant.

nature portfolio

Corresponding author(s): Hiro Furukawa

Last updated by author(s): Sep 24, 2025

Reporting Summary

Nature Portfolio wishes to improve the reproducibility of the work that we publish. This form provides structure for consistency and transparency in reporting. For further information on Nature Portfolio policies, see our Editorial Policies and the Editorial Policy Checklist.

Statistics

For all statistical analyses, confirm that the following items are present in the figure legend, table legend, main text, or Methods section.

n/a	Confirmed	
☐	☒	The exact sample size (*n*) for each experimental group/condition, given as a discrete number and unit of measurement
☐	☒	A statement on whether measurements were taken from distinct samples or whether the same sample was measured repeatedly
☐	☒	The statistical test(s) used AND whether they are one- or two-sided *Only common tests should be described solely by name; describe more complex techniques in the Methods section.*
☒	☐	A description of all covariates tested
☐	☒	A description of any assumptions or corrections, such as tests of normality and adjustment for multiple comparisons
☐	☒	A full description of the statistical parameters including central tendency (e.g. means) or other basic estimates (e.g. regression coefficient) AND variation (e.g. standard deviation) or associated estimates of uncertainty (e.g. confidence intervals)
☐	☒	For null hypothesis testing, the test statistic (e.g. *F*, *t*, *r*) with confidence intervals, effect sizes, degrees of freedom and *P* value noted *Give P values as exact values whenever suitable.*
☒	☐	For Bayesian analysis, information on the choice of priors and Markov chain Monte Carlo settings
☒	☐	For hierarchical and complex designs, identification of the appropriate level for tests and full reporting of outcomes
☒	☐	Estimates of effect sizes (e.g. Cohen's *d*, Pearson's *r*), indicating how they were calculated

Our web collection on statistics for biologists contains articles on many of the points above.

Software and code

Policy information about availability of computer code

Data collection	EPU 2.10.0.5 was used for Cryo-EM data collection. PatchMaster v2x32 and Clampex 10.7 were used for electrophysiological data collection.
Data analysis	CryoSPARC 4.6.2 were used for Cryo-EM single-particle analysis. PHENIX 1.20.1, winCOOT 0.9.8.95, ChimeraX 1.4 and Pymol 3.1 were used for model building, refinement and analysis. Hole 2.2 was used for pore analysis. Excel 2016 and GraphPad Prism 10 were used for TEVC electrophysiological data analysis. Origin 8,OriginPro 2022b, and GraphPad Prism 10 were used for single-channel electrophysiological data analysis. For MD simulation, Modeller 9.12, Antechamber, Gromacs 2021.3, LINCS algorithm, Python 3.0, and Open MM version 7.5.1 were used for fixing residues, ligand parameterization, setting up/performing simulations, analysis, and unbiased simulations, respectively.

For manuscripts utilizing custom algorithms or software that are central to the research but not yet described in published literature, software must be made available to editors and reviewers. We strongly encourage code deposition in a community repository (e.g. GitHub). See the Nature Portfolio guidelines for submitting code & software for further information.

Data

Policy information about availability of data

All manuscripts must include a data availability statement. This statement should provide the following information, where applicable:

- Accession codes, unique identifiers, or web links for publicly available datasets
- A description of any restrictions on data availability
- For clinical datasets or third party data, please ensure that the statement adheres to our policy

Cryo-EM data are deposited to dedicated PDB/EMDB ID; non-active state Gly, Glu, PS bound hGluN1a-2B NMDAR (PDB:9OOS. EMDB: EMD-70671), pre-active state Gly, Glu, PS bound hGluN1a-2B NMDAR (PDB: 9OOT. EMDB: EMD-70672), closed state Gly, Glu, 24S-HC bound hGluN1a-2B NMDAR (PDB: 9OOQ. EMDB: EMD-70669), open state Gly, Glu, 24S-HC bound hGluN1a-2B NMDAR (PDB: 9OOR. EMDB: EMD-70671), and sub-open state Gly, Glu, EU1622-240 bound rGluN1a-2B NMDAR (PDB: 9OOU. EMDB: EMD-70673). Electrophysiological data are available upon reasonable request.

Research involving human participants, their data, or biological material

Policy information about studies with human participants or human data. See also policy information about sex, gender (identity/presentation), and sexual orientation and race, ethnicity and racism.

Reporting on sex and gender	N/A
Reporting on race, ethnicity, or other socially relevant groupings	N/A
Population characteristics	N/A
Recruitment	N/A
Ethics oversight	N/A

Note that full information on the approval of the study protocol must also be provided in the manuscript.

Field-specific reporting

Please select the one below that is the best fit for your research. If you are not sure, read the appropriate sections before making your selection.

☒ Life sciences ☐ Behavioural & social sciences ☐ Ecological, evolutionary & environmental sciences

For a reference copy of the document with all sections, see nature.com/documents/nr-reporting-summary-flat.pdf

Life sciences study design

All studies must disclose on these points even when the disclosure is negative.

Sample size	Sample sizes were not predetermined in this study. The sample sizes of Cryo-EM data were determined based on the convergence of structural resolution. The data of the electrophysiological experiments were repeated at least six times.
Data exclusions	In cryo-EM single-particle analysis, particles in 2D and 3D classes which did not possess high-resolution features were removed in the final 3D reconstruction.
Replication	Cryo-EM related experiments including protein expression, purification were reproduced at least three times independently. Cryo-EM data collections for each condition were performed at least two times in two different dates. Electrophysiology experiments were repeated at least on six independent oocytes. All electrophysiological recording attempts at replication were successful.
Randomization	In cryo-EM related experiments, all micrograph movies were acquired in random places on the EM grids and particles were randomly partitioned for resolution and quality assessment in single-particle analysis. Electrophysiological experiments were not randomized. Covariant control was not possible since we transfected pre-determined DNA constructs and optimize expression to maximize successful recording for each construct.
Blinding	Blinding was not conducted for cryo-EM single-particle analysis. To achieve this, multiple datasets by many scientists would need to be recruited. Such an experimental mechanism for cryo-EM would not be feasible with the federal budget. For electrophysiology, the same scientists were responsible for conducting molecular biology, cell culture, and electrophysiology. This was inevitable to acquire high-quality results. The above situations made blinding not feasible.

Reporting for specific materials, systems and methods

We require information from authors about some types of materials, experimental systems and methods used in many studies. Here, indicate whether each material, system or method listed is relevant to your study. If you are not sure if a list item applies to your research, read the appropriate section before selecting a response.

Materials & experimental systems

n/a	Involved in the study
☒	☐ Antibodies
☐	☒ Eukaryotic cell lines
☒	☐ Palaeontology and archaeology
☒	☐ Animals and other organisms
☒	☐ Clinical data
☒	☐ Dual use research of concern
☒	☐ Plants

Methods

n/a	Involved in the study
☒	☐ ChIP-seq
☒	☐ Flow cytometry
☒	☐ MRI-based neuroimaging

Eukaryotic cell lines

Policy information about cell lines and Sex and Gender in Research

Cell line source(s)	Sf9 insect cells used in the study were provided by Cold Spring Harbor Laboratory. Xenopus oocytes were either harvested from the frogs raised in the animal facilities of Cold Spring Harbor Laboratory or purchased from Ecocyte Bioscience. HEK293T used in this study was acquired from ATCC Cat#CRL-3216.
Authentication	The cells were routinely maintained in our laboratory They were not authenticated for these cell lines.
Mycoplasma contamination	The cell lines were tested negative for mycoplasma contamination.
Commonly misidentified lines (See ICLAC register)	No commonly misidentified lines were used in this study.

Plants

Seed stocks	N/A
Novel plant genotypes	N/A
Authentication	N/A